

Geochemistry of shear zone-hosted uranium mineralisation at the Zadní Chodov uranium deposit (Bohemian Massif)

Martina Havelcová^{a,*}, Vladimír Machovič^{a,b}, Miloš René^a, Ivana Sýkorová^a, Ladislav Lapčák^b, Alexandra Špaldoňová^a

^a Institute of Rock Structure and Mechanics, AS CR, V Holešovičkách 41, 182 09 Prague 8, Czech Republic

^b University of Chemistry and Technology, Prague, Technická 5, 166 28 Prague 6, Czech Republic



ARTICLE INFO

Keywords:

Brannerite
Graphite
Uranium
Organic matter
Bohemian Massif
Micro-Raman spectroscopy

ABSTRACT

Samples from the Zadní Chodov uranium deposit of the Bohemian Massif were analysed using optical and chemical methods. Organic matter and brannerite were studied in detail to estimate conditions that prevailed in association with uranium-enriched shear zones. Four major events are known in the high-grade metasediments. The pre-ore stage is associated with the formation of shear zones. During the uranium ore deposition stage, temperatures ranged from 122 °C to 258 °C, and coffinite and brannerite appeared. Two generations of post-ore stage minerals are distinguishable. A detailed study of a brannerite mineral grain revealed variations in its interior and surroundings, but these are related to the composition of brannerite, which is not a nominal mineral. Si and Al are presented as chlorites, but the main mineral phases are mixtures of anatase, oxidized brannerite with non-stoichiometric uranium oxide, and carbonaceous matter. Carbonaceous matter in the samples studied appeared as a mixture of substances of different composition, origin, and age. Optical and structural characteristics showed variations in three coexisting types of metamorphosed carbonaceous matter, including fine-grained and larger lamella-shaped particles that represent anthracite, meta-anthracite and semi-graphite stages, lamellas of crystalline graphite, and pyrobitumen, corresponding to imponite. The structure of organic particles was not affected by uranium minerals, which is an interesting difference from changes that minerals undergo in, for example, coal. Biomarkers, compounds used in assessing sources of organic matter, were present in extracts, but they were not a remnant of the original shear zone organic material. They are likely products from a later impact, probably of Tertiary and younger sediments.

1. Introduction

The total amount of extracted uranium, approximately 350 000 tons (OECD-IAEA, 2003), makes the Bohemian Massif the most important uranium ore district in the European Variscan belt. The most important genetic type of uranium deposit is represented by vein-type uranium mineralisation (50,000 t U at Příbram, 8500 t U at Jáchymov). The other significant genetic type is shear-zone hosted uranium mineralisation in the Moldanubian Zone (4200 t U at Zadní Chodov, 20,000 t U at Rožná). The shear-zone hosted uranium mineralisation is usually connected with organic matter-enriched filling of these mineralised shear zones (Dill, 1985, 1986; Křibek, 1989; Křibek et al., 2009; Dill et al., 2019).

Biogenic carbonaceous matter is common in many types of sedimentary rocks. During regional metamorphism, it changes in structure from turbostratic amorphous to crystalline hexagonal graphite. Possible

alterations in the graphite during retrograde metamorphism or the influence of circulating hydrothermal fluids were documented (Frost 1988; Wang et al., 1989). Although in several works the authors have characterized graphite as chemically and thermally inert, with stable structural arrangements up to approximately 400 °C, several studies have described alterations of graphite at temperatures around 250 °C (Gautneb and Tveten, 2000; Schiffbauer et al., 2007). Generally, it is believed that alteration of graphite is affected by uranium mineralisation, as well as circulation of hydrothermal fluids (Kyser et al., 1989).

The aim of this study is to analyse in detail the organic matter in uranium enriched shear zones of the Zadní Chodov uranium deposit. The petrology and chemical composition of different organic matter in mineralised shear zones were analysed using optical microscopy and spectrophotometry of dispersed organic matter, and gas chromatography/mass spectrometry (GC/MS) and micro-Raman spectroscopy were used to estimate the original organic matter, as well as possible

* Corresponding author.

E-mail address: havelcova@irms.cas.cz (M. Havelcová).

<https://doi.org/10.1016/j.oregeorev.2020.103428>

Received 7 August 2019; Received in revised form 11 February 2020; Accepted 19 February 2020

Available online 20 February 2020

0169-1368/ © 2020 Elsevier B.V. All rights reserved.

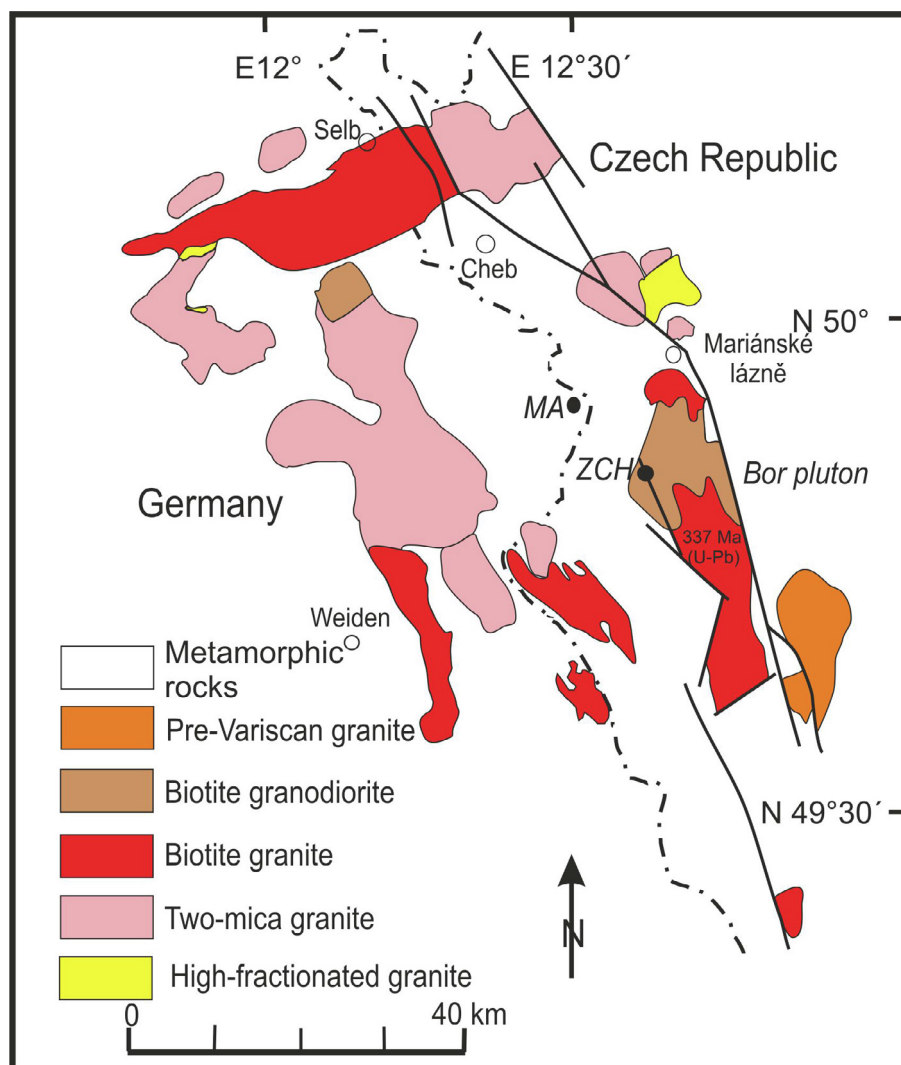


Fig. 1. Geological map of granitoids in the western part of the Bohemian Massif. ZCH – Zadní Chodov uranium deposit, MA – Mähring uranium deposit (modified by M. René after Breiter and Sokol, 1997; Siebel et al., 1997).

conditions that prevailed during the origin of uranium enriched shear zones. Micro-Raman spectroscopy was also used for a detailed study of brannerite.

2. Geological setting

The Zadní Chodov uranium deposit is located on the northwestern margin of the Bor pluton, which intruded into the West Bohemian shear zone (Zulauf, 1994) at the boundary between the Moldanubian and Teplá-Barrandian zones during the Variscan magmatic event (337 ± 6 Ma, U/Pb TIMS analyses on zircon; Dörr et al., 1997) (Fig. 1). The Zadní Chodov uranium deposit was mined from 1952 to 1992 and was ranked as a medium-size uranium deposit in the Bohemian Massif. The total mine production of low-grade uranium ore (0.195 wt% U) was 4151 t U (Kafka, 2003). The deposit, which is located in the northern tectonic block of the Bor pluton, was investigated by mine workings to a depth of 1250 m over a strike length of more than 2.5 km. The contact with the Moldanubian high-grade metasediments was tectonic, comprising several shear structures parallel to the Zadní Chodov shear zone, which forms the western boundary of the Bor pluton (Fig. 2). Migmatized biotite paragneiss of the Moldanubian Varied Group dominates. It contains intercalated quartzites, amphibolites, calc-silicate rocks and crystalline limestones. Dykes and bodies of amphibole-biotite tonalites and biotite granites cut the paragneiss.

Aplite, pegmatite, and lamprophyre dykes are less frequent, particularly present above and below large shear zones. Uranium mineralisation was associated with the N-S trending zones of the Zadní Chodov fault at the intersection with NW-SE trending fault structures, which form an NW continuation of the Central fault.

The Zadní Chodov shear zone has been verified to exceed 20 km, its width in the middle section reaches 500 m, dipping $50\text{--}75^\circ$ to the east. This dislocation passed northwards into the Eastern shear zone of the Zadní Chodov deposit (Fig. 3). The shear zones consist of intensely altered and crushed rocks with chlorite-rich and/or clay-mineral-rich assemblages. Uranium mineralisation occurs in three shear zones (CH-1, CH-11, and CH-12), and the width of individual shear zones was highly variable from 30 cm to approximately 1–2.5 m. The total width of these mineralised shear zones was 50–150 m. High-grade uranium mineralisation was developed at depths of 440–960 m beneath the present surface, and the most common uranium minerals were coffinite (65 vol%), uraninite (25 vol%), and brannerite (10 vol%). The uranium mineralisation of the main ore stage was dated at 260 ± 2 Ma based on the U–Pb age of uraninite, obtained by isotope dilution-thermal ionization mass spectrometry (ID-TIMS). The U–Pb age of brannerite is 185 ± 6 Ma (ID-TIMS), and was interpreted as the Mesozoic re-crystallisation of brannerite during the main ore stage (Ordynec et al., 1987).

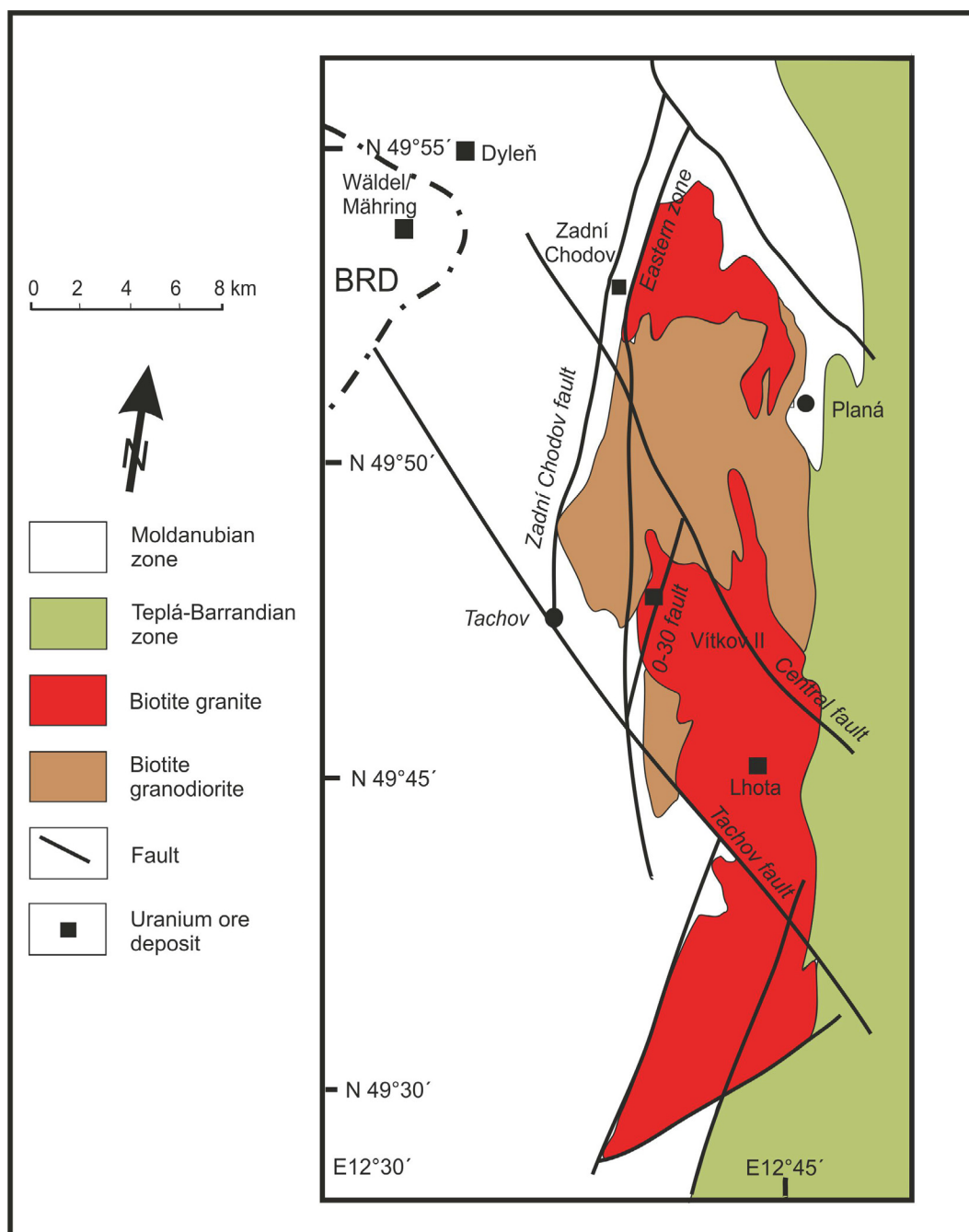


Fig. 2. Geological map of the Bor pluton (modified by M. René after Holovka and Hnízdo, 1992).

3. Samples and methods

Five representative samples of the mineralised shear zone infill, located in the lowest part of the uranium deposit (23 level), were studied (ZCH-8, ZCH-31, ZCH-94, ZCH-95, ZCH-102).

The distribution, morphology, and reflectance of carbonaceous particles were studied and measured on polished sections of rock slabs oriented perpendicular to banding or foliation of the rock samples. The morphological types of high-reflecting carbonaceous matter, including fine granular, lamella-like and dense particles of semi-graphite, graphite, and bitumen were identified in accordance with definitions outlined in Kwiecińska and Petersen (2004), Kříbek et al. (2008), Jacob (1993), and determined by an Olympus BX51 incident light microscope with Zeiss Photomultiplier MK3, and a Pelcon point counter. Reflectance measurements of organic matter were made according to ISO

7404-5 (2009) using a Carl Zeiss Axio Imager M2m incident light microscope with a cooled CCD spectrometer under the following conditions: oil lenses (magnification of $50 \times$ and $100 \times$), wave length of 546 nm, non-drying oil immersion ($n = 1.518$). Random reflectance measurements of lamella-like morphology, dense particles and the fine granular forms of carbonaceous matter (R_r ; in %) were made in normal light while measurements of maximum (R_{max} ; in %) and minimum (R_{min} ; in %) reflectance were performed in polarized light using yttrium–aluminium–garnet ($R = 0.900\%$), gadolinium–gallium–garnet ($R = 1.717\%$), cubic zirconia ($R = 3.12\%$), and strontium–titanate ($R = 5.41\%$) reflectance standards.

Rock-forming and uranium minerals were analysed in polished thin sections using a CAMECA SX 100 electron microprobe operated in wavelength-dispersive mode. The accelerating voltage and beam currents were 15 kV and 15nA, with a $2 \mu\text{m}$ beam diameter. Calibrations

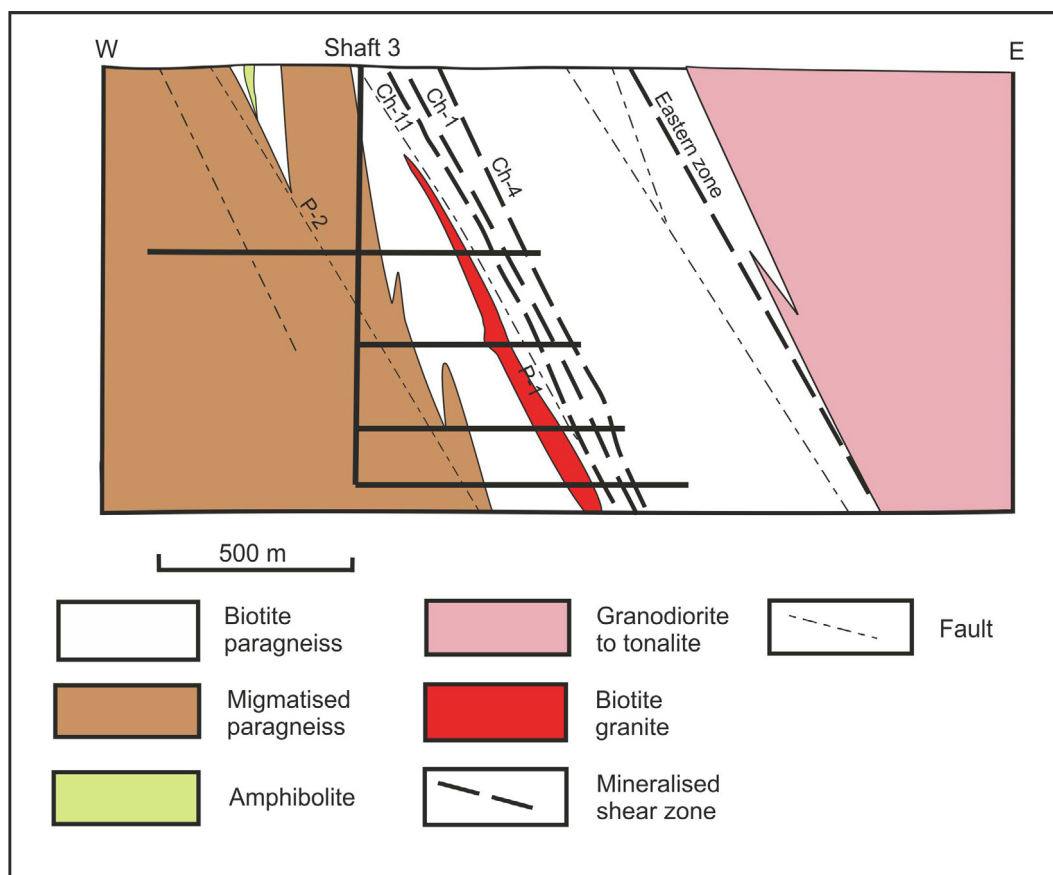


Fig. 3. Schematic geological cross-section of the Zadní Chodov uranium deposit (modified by M. René after Novák and Paška, 1983).

were carried out using standard sets from SPI Supplies. The raw data were corrected using PAP matrix corrections (Pouchou and Pichoir, 1985). For chlorite thermometry, the six-component chlorite solid solution model of Walshe (1986) was used.

Whole-rock samples enriched in clay minerals were chosen to sample the clay mineral fraction. The fraction of clay minerals below 4 μm was prepared using a conventional sedimentation method. X-ray diffraction (XRD) analyses of clay minerals were obtained on randomly oriented and sedimented samples that were air-dried, untreated, ethylene glycol solvated and heated (500 $^{\circ}\text{C}$, 700 $^{\circ}\text{C}$) using a Bruker D8 Discover diffractometer with $\text{CuK}\alpha$ radiation (40 kV, 40 mA), Ni filter standard set, scanning speed 1 $^{\circ}$ /min, step size 0.02 and spreading between 3 and 35 $^{\circ}$ 2 θ for oriented samples.

Raman spectra were measured using a Thermo Scientific DXR Raman microscope equipped with a 532 nm line laser. An optical camera was used to examine locations of interest on polished samples. The spot size of the laser focused using the 50 \times objective was \sim 1 μm in diameter. A laser power of 10 mW was used to obtain high quality Raman spectra allowing the production of spectral maps. Scattered light was analysed by a spectrograph with holographic grating (400 lines per mm) and a pinhole width of 50 μm . The acquisition time was 1 s. Four accumulations were added together to obtain a spectrum. A 1 μm step was selected for microspectroscopic surface mapping using the OMNIC Atlas imaging software program (Thermo Fisher Scientific) and 7040 spectra were obtained from an area of 80 \times 88 μm . From the measured spectra, correlation 2D maps were calculated on the basis of spectral features of individual spectra in the map compared with spectral characteristics of a chosen standard. A clean component is usually used as the standard but in the case of this study, a characteristic mixture of components forming individual layers, grains or surrounding matrix was used (e.g. chlorite, hydroxyapatite, graphite). The spectra were

fitted with a mixed Gauss-Lorentz function.

Structural parameters of carbonaceous matter were characterised by the first-order Raman spectra of samples, where two prominent features dominated. The G band corresponds to stretching vibrations of the E_{2g} mode in graphitic aromatic layers. The D1 band was assigned to the graphite lattice A_{1g} mode and is connected with planar defects between the basic structural units or the presence of heteroatoms (Tuinstra and Koenig, 1970). Positions, full width at half maximum (FWHM) and the intensity ratio of both bands are parameters that can describe the structure of a carbonaceous material. The D and G bands of carbonaceous matter were curve-fitted using the Lorentzian function, and FWHM of the D band, the R1 (I_D/I_G) intensity ratio and R2 ($A_D/(A_D + A_G)$) area ratio were used as parameters proportional to the degree of graphitization of carbonaceous samples (Tuinstra and Koenig, 1970; Ferrari and Robertson, 2000).

The samples were crushed to a grain size less than 0.1 mm, dried and powdered before chemical analyses. The elemental organic composition was determined using a CHNS/O, Thermo Finnigan Flash FA 1112 microanalyser. Total organic carbon (TOC) was determined by elemental analysis after elimination of inorganic carbonates using 1 N HCl heated to 80 $^{\circ}\text{C}$.

The powdered samples (about 12 g) were Soxhlet-extracted (Büchi B-811) with dichloromethane and methanol (1:1 v/v) for 6 h. Elemental sulphur was removed by addition of activated copper sheets to the flask for 8 h. The extracts were filtered through a glass fibre filter and concentrated using a Christ RVC 2–18 rotator evaporator. The total extracts were redissolved in 1.5 ml dichloromethane and methanol (1:1 v/v). Due to the low contents of organic carbon, the extracts were not further separated into fractions of saturated and aromatic hydrocarbons, and the whole extract was analysed by GC/MS.

GC/MS analyses were performed on a Trace GC Ultra - DSQ II

system (ThermoScientific) fitted with a DB-5 capillary column (30 m, 0.25 mm inner diameter, 0.25 μm film thickness). The GC operating conditions were as follows: 36 °C held for 2 min, then ramped at 15 °C/min until 120 °C, ramped at 6 °C/min until 250 °C, ramped at 12 °C/min until 300 °C and then held for 6 min. Samples (1 μL) were injected in splitless mode with the injector temperature at 220 °C. Helium was used as the carrier gas. The MS was operating in the electron impact mode at ionisation energy of 70 eV. Mass spectra were obtained by scanning from 45 to 650 amu in full scan mode. Data were acquired and processed with Xcalibur software (Thermo Electron). Individual compounds were assigned from retention time and identification of compounds was based on comparison of standard spectra from the National Institute of Standards and Technology mass spectral library.

4. Results

4.1. Petrography of metasediments

Metasediments from the Zadní Chodov uranium deposits consisted predominantly of partly migmatized biotite paragneisses, sillimanite-biotite paragneisses, biotite quartzitic paragneisses and cordierite-biotite paragneisses. The dominant biotite and quartzitic biotite paragneisses were medium- to fine-grained rocks, containing quartz, plagioclase, biotite, and K-feldspar. The amount of anorthite in the plagioclases from these high-grade metamorphosed sediments ranged from An₂₀ to An₃₅. Garnet was found occasionally, and accessory minerals were represented by apatite, ilmenite, zircon, monazite, titanite, and xenotime.

4.2. Petrography of altered metasediments

Four major stages of alteration of metasediments can be distinguished, namely pre-ore, syn-ore and two post-ore stages (Mrázek and Fiala, 1979; Fig. 4).

The pre-ore stage in high-grade metamorphic rocks is associated with the formation of shear zones. The appearance of shear zones is accompanied by the accumulation of organic matter and/or clay minerals together with chloritisation of original biotite (chlorite I). In the fine-grained infilling of shear zones, chlorite I (Fe/(Fe + Mg) = 0.30–0.67) dominated over illite. Together with chloritisation of biotite muscovite I, hematite, anatase and/or very rare broockite developed. Original plagioclase was albitised (albite I, An_{0.0–0.9}), and monazite was partly altered into Th-depleted monazite and thorite.

During the syn-ore stage, chlorite II, apatite, coffinite, and brannerite appeared. Chlorite II (Fe/(Fe + Mg) = 0.12–0.33) formed well crystallised aggregates in the fine-grained infilling of the shear zones. Apatite appeared in relatively large irregular grains in this fine-grained infilling of chlorite and clay minerals. In some cases, during the ore stage, very fine veinlets of quartz I developed.

The post-ore quartz stage is related to the origin of small veins and veinlets of uraninite II and quartz II. During the post-ore carbonate stage, calcite, dolomite, and ankerite appeared, together with a small amount of sulphides (pyrite, chalcocopyrite, galenite, and sphalerite) and selenides (e.g., clausthalite, poubaite, nevskite).

4.3. Chlorite thermometry

The authigenic chlorite data (chlorite II) were used to calculate the temperature of alteration during the syn-ore stage. The chlorite II crystal chemistry indicates that the temperature ranged from 122 °C to 258 °C.

4.4. Composition and Raman microspectroscopy of brannerite

In the Zadní Chodov ore deposit, especially in samples from the

| Stage | Pre-ore | Ore | Post-ore quartz | Post-ore carbonate |
|---------------------|---------|-----|-----------------|--------------------|
| Chlorite | I | II | III | |
| Anatase | | | | |
| Titanite | | | | |
| Albite | I II | | | |
| Muscovite | | | | |
| Illite | | | | |
| Kaolinite | | | | |
| Carbonaceous matter | | | | |
| Hematite | | | | |
| Quartz | | I | II III | |
| Apatite | | | | |
| Brannerite | | I | II | |
| Coffinite | | | | |
| Uraninite | | I | II | |
| Thorite | | | | |
| Calcite | | | | |
| Dolomite | | | | |
| Pyrite | | | | |
| Chalcocopyrite | | | | |
| Galena | | | | |
| Fluorite | | | | |
| Selenides | | | | |
| Zeolites | | | | |

Fig. 4. Paragenetic sequence of the hydrothermal mineralisation. Compiled after Mrázek and Fiala, 1979; Fiala, 1980a,b; Arapov et al., 1984 and results of the present study.

lowest level 23, uranium mineral of the highest economic interest was brannerite. The brannerite occurred as needle crystal aggregates and/or irregular grains. Larger brannerite grains were usually heterogeneous, metamictised and, on the rim, altered into Ti-enriched brannerite and anatase. Smaller brannerite grains were often entirely altered into Ti-enriched brannerite and anatase (Fig. 5). The composition of representative unaltered and partly altered brannerite samples is shown in Table 1.

The range of unaltered and/or partly altered brannerite, based on all analyses obtained in this study, indicate that it contained 32.1–38.3 wt% TiO₂, 1.9–34.4 wt% UO₂, 17.4–34.4 wt% UO₃, 0.0–2.8 wt% ThO₂, 0.9–4.5 wt% CaO, 0.0–1.4 wt% PbO, 0.0–0.02 wt% Nb₂O₅, 0.0–1.4 wt% SiO₂, 0.0–0.5 wt% Al₂O₃, 0.7–2.2 wt% FeO, 0.2–2.2 wt% Y₂O₃, 0.1–0.5 wt% ZrO₂ and 0.0–0.2 wt% REE₂O₃. The highly altered brannerite was depleted in U and enriched in Ti, Si, and Al. The chemical formula of brannerite was initially calculated from the microprobe analyses by normalisation to 6.0 oxygens. On this basis, total cations commonly exceeded the ideal value of 3.0, indicating that

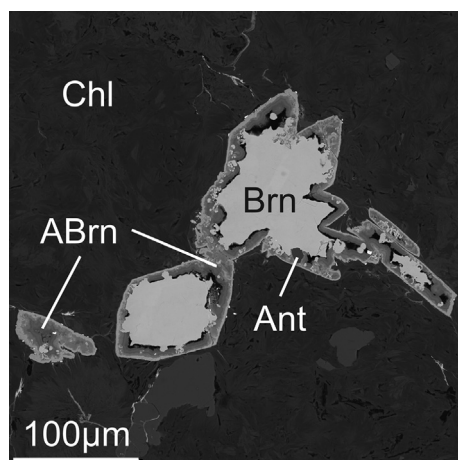


Fig. 5. Back-scattered electron microscope images of brannerite (Brn), altered brannerite (ABrn), and anatase (Ant) enclosed in fine-grained chlorite (Chl).

Table 1

Representative analyses of brannerite in sample ZCH-8 (Zadní Chodov, level 23, gallery V-23).

| wt% | 22 | 24 | 25 | 27 | 28 | 29 | 31 | 33 |
|--------------------------------|--------|-------|-------|-------|-------|-------|-------|--------|
| UO ₂ | 28.16 | 34.32 | 28.63 | 34.38 | 25.68 | 29.44 | 28.50 | 28.98 |
| UO ₃ | 25.72 | 19.08 | 25.44 | 21.20 | 27.22 | 26.38 | 26.40 | 25.44 |
| ThO ₂ | 0.24 | 0.11 | 0.01 | 0.06 | 0.04 | 0.04 | 0.19 | 0.14 |
| TiO ₂ | 38.33 | 37.57 | 37.33 | 37.46 | 37.39 | 36.73 | 36.45 | 37.38 |
| FeO | 1.63 | 1.84 | 1.28 | 1.67 | 1.78 | 2.02 | 1.48 | 1.97 |
| CaO | 2.92 | 2.74 | 2.72 | 2.70 | 2.96 | 2.50 | 2.99 | 3.27 |
| MnO | 0.49 | 0.39 | 0.45 | 0.38 | 0.48 | 0.47 | 0.42 | 0.47 |
| SiO ₂ | 0.02 | 0.06 | 0.24 | 0.01 | 0.05 | 0.02 | 0.61 | 0.30 |
| ZrO ₂ | 0.49 | 0.35 | 0.18 | 0.05 | 0.29 | 0.08 | 0.19 | 0.33 |
| Sc ₂ O ₃ | 0.83 | 0.36 | 0.23 | 0.23 | 0.35 | 0.31 | 0.28 | 0.22 |
| Nb ₂ O ₅ | 0.05 | 0.04 | 0.11 | 0.06 | 0.06 | 0.09 | 0.15 | 0.06 |
| Al ₂ O ₃ | 0.00 | 0.00 | 0.00 | 0.00 | 0.01 | 0.00 | 0.29 | 0.03 |
| PbO | 0.03 | 0.00 | 0.00 | 0.00 | 0.01 | 0.02 | 0.05 | 0.00 |
| Ce ₂ O ₃ | 0.23 | 0.20 | 0.25 | 0.25 | 0.47 | 0.25 | 0.28 | 0.25 |
| Pr ₂ O ₃ | 0.16 | 0.00 | 0.02 | 0.03 | 0.16 | 0.05 | 0.04 | 0.04 |
| Nd ₂ O ₃ | 0.10 | 0.16 | 0.35 | 0.36 | 0.71 | 0.17 | 0.15 | 0.43 |
| Sm ₂ O ₃ | 0.20 | 0.15 | 0.24 | 0.15 | 0.27 | 0.14 | 0.16 | 0.21 |
| Gd ₂ O ₃ | 0.10 | 0.20 | 0.15 | 0.08 | 0.14 | 0.09 | 0.24 | 0.08 |
| Tb ₂ O ₃ | 0.00 | 0.02 | 0.05 | 0.04 | 0.00 | 0.01 | 0.03 | 0.00 |
| Dy ₂ O ₃ | 0.06 | 0.00 | 0.22 | 0.17 | 0.17 | 0.13 | 0.04 | 0.04 |
| Er ₂ O ₃ | 0.00 | 0.03 | 0.00 | 0.07 | 0.02 | 0.08 | 0.10 | 0.11 |
| Yb ₂ O ₃ | 0.01 | 0.02 | 0.09 | 0.11 | 0.06 | 0.01 | 0.05 | 0.07 |
| Y ₂ O ₃ | 0.30 | 0.42 | 0.51 | 0.44 | 0.51 | 0.44 | 0.40 | 0.41 |
| Total | 100.07 | 98.06 | 98.50 | 99.90 | 98.83 | 99.47 | 99.49 | 100.23 |
| apfu | | | | | | | | |
| U ⁴⁺ | 0.41 | 0.52 | 0.43 | 0.51 | 0.38 | 0.44 | 0.42 | 0.41 |
| U ⁶⁺ | 0.34 | 0.26 | 0.36 | 0.29 | 0.37 | 0.38 | 0.37 | 0.34 |
| Ti ⁴⁺ | 1.84 | 1.87 | 1.84 | 1.85 | 1.82 | 1.81 | 1.78 | 1.81 |
| Fe ²⁺ | 0.09 | 0.10 | 0.07 | 0.09 | 0.10 | 0.11 | 0.08 | 0.11 |
| Ca ²⁺ | 0.20 | 0.19 | 0.19 | 0.19 | 0.21 | 0.18 | 0.21 | 0.23 |
| Mn ²⁺ | 0.03 | 0.02 | 0.02 | 0.02 | 0.03 | 0.03 | 0.02 | 0.03 |
| Si ⁴⁺ | 0.00 | 0.00 | 0.02 | 0.00 | 0.00 | 0.00 | 0.04 | 0.02 |
| Zr ⁴⁺ | 0.02 | 0.01 | 0.01 | 0.00 | 0.01 | 0.00 | 0.01 | 0.01 |
| Sc ³⁺ | 0.05 | 0.02 | 0.01 | 0.01 | 0.02 | 0.02 | 0.02 | 0.01 |
| Al ³⁺ | 0.00 | 0.00 | 0.00 | 0.00 | 0.00 | 0.00 | 0.02 | 0.00 |
| Ce ³⁺ | 0.01 | 0.00 | 0.01 | 0.01 | 0.01 | 0.01 | 0.01 | 0.01 |
| Nd ³⁺ | 0.00 | 0.00 | 0.01 | 0.01 | 0.02 | 0.00 | 0.00 | 0.01 |
| Sm ³⁺ | 0.00 | 0.00 | 0.01 | 0.00 | 0.01 | 0.00 | 0.00 | 0.00 |
| Gd ³⁺ | 0.00 | 0.00 | 0.00 | 0.00 | 0.00 | 0.00 | 0.01 | 0.00 |
| Y ³⁺ | 0.01 | 0.01 | 0.02 | 0.02 | 0.02 | 0.02 | 0.01 | 0.01 |
| O | 6 | 6 | 6 | 6 | 6 | 6 | 6 | 6 |

a significant amount of U must be in a higher valence state than the assumed U⁴⁺ state. Therefore, the analyses were re-normalised to 3.0 cations and the amount of U⁶⁺ necessary to provide charge was recalculated.

To analyse this very complex material thoroughly, Raman mapping

microspectroscopy was appropriate because the measurement step is of the order of microns. Correlation 2D maps, describing the distribution of the present mineral phases and carbonaceous matter, were created for a grain of about 40x80 µm in size (specifically sample ZCH-8). From the four characteristic Raman spectra (Fig. 6) and the microphotography of the mapped grain with phase correlation maps (Fig. 7), one can get an idea of the complex structure of the brannerite grain and its surroundings, about the distribution of individual mineral phases in the grain layers, and the layer thickness.

The outer annular rim, about 3–4 µm wide, which forms the upper envelope of the grain (spectrum and map A in Figs. 6 and 7) is composed of anatase (147, 200, 395, 517 cm⁻¹), brannerite (162, 323, 565, 594, 675 cm⁻¹), and carbonaceous matter (1587, 1358 cm⁻¹ not shown in spectra). Positions and half-widths of the bands corresponded well with those of Zhang et al. (2013) (Table 2).

Between the core and the outer grain layer, there was a thinner layer, about 1–2 µm wide (spectrum and map B in Figs. 6 and 7), formed by a relatively amorphous brannerite with broad bands of Ti-O and U-O stretching vibrations. Brannerite was partially oxidized and contained UO₂²⁺ cations (814, 876 cm⁻¹). The relatively intense band at 247 cm⁻¹ was probably caused by U-O modes of non-stoichiometric uranium oxide.

The grain core (spectrum and map C in Figs. 6 and 7) consists of a mixture of amorphous brannerite with UO₂²⁺, UO_{2.12}, and TiO₂ (anatase). The spectrum and map D in Figs. 6 and 7 describe the occurrence of crystalline brannerite, which contained highly graphitized carbonaceous material.

In addition to the mineral phases described above, further phases were found in the surrounding matrix and also partly in the grain. The dominant phase surrounding and intervening in the grain was chlorite (Fig. 8A and C). The spectrum exhibited bands characteristic of asymmetric (1002 cm⁻¹) and symmetric (681 cm⁻¹) Si-O-Si stretching and Si-O bending (550, 432, 357 cm⁻¹) modes. The bands at 432, 357, 293, 203, 137 and 102 cm⁻¹ were assigned to translational Me-O modes (Gopal et al., 2004). The hydroxyapatite content (Ca₁₀(PO₄)₆(OH)₂) (Fig. 8B) was relatively low, and the Raman spectrum (Fig. 8D) showed an intense sharp symmetrical vibration band of the PO₄ group at 965 cm⁻¹. The bands at 1043, 1053 and 1149 cm⁻¹ belonged to the antisymmetric stretching vibrations of PO₄ or symmetric CO₃ stretching modes. Bending vibrations of PO₄ were found at 591, 582 and 431 cm⁻¹ and lattice modes about 140 cm⁻¹ (Wopenka and Pasteris, 2005). Furthermore, small amounts of brookite (rutile was not detected) and pyrite were identified in the matrix by Raman spectroscopy.

4.5. Carbonaceous matter

The samples of altered high-grade metasediments (ZCH-8, ZCH-31, ZCH-94, ZCH-95 and ZCH-102) contained only small amounts of minute carbonaceous particles with random reflectance changing between 3.39% and 7.33% (Table 3). Carbonaceous particles, ranging in size from about 1 µm to about 200 µm, occurred along microscopic cracks and gaps between the crystals and grains of minerals. In samples ZCH-31 and ZCH-95, the irregular clumps around microscopic cracks were much larger. Three types of high-reflecting carbonaceous particles were distinguished according to their morphologies and reflectance values.

Type I particles (Table 3) were fine-grained, irregular or elongated bodies with an average size-length up to 10 µm. They filled microcracks in the form of thin lines, or formed irregular aggregates that were dispersed in the inorganic matrix (Fig. 9A). Maximum reflectance values were often difficult to obtain due to the small particle size. However, average R_{max} values ranged between 2.62% and 5.88%, which corresponded to the anthracite, meta-anthracite, and rare graphite stage.

Type II particles were of elongated and lamellar shapes, commonly arranged parallel to the shear and in contact with two mineral phases

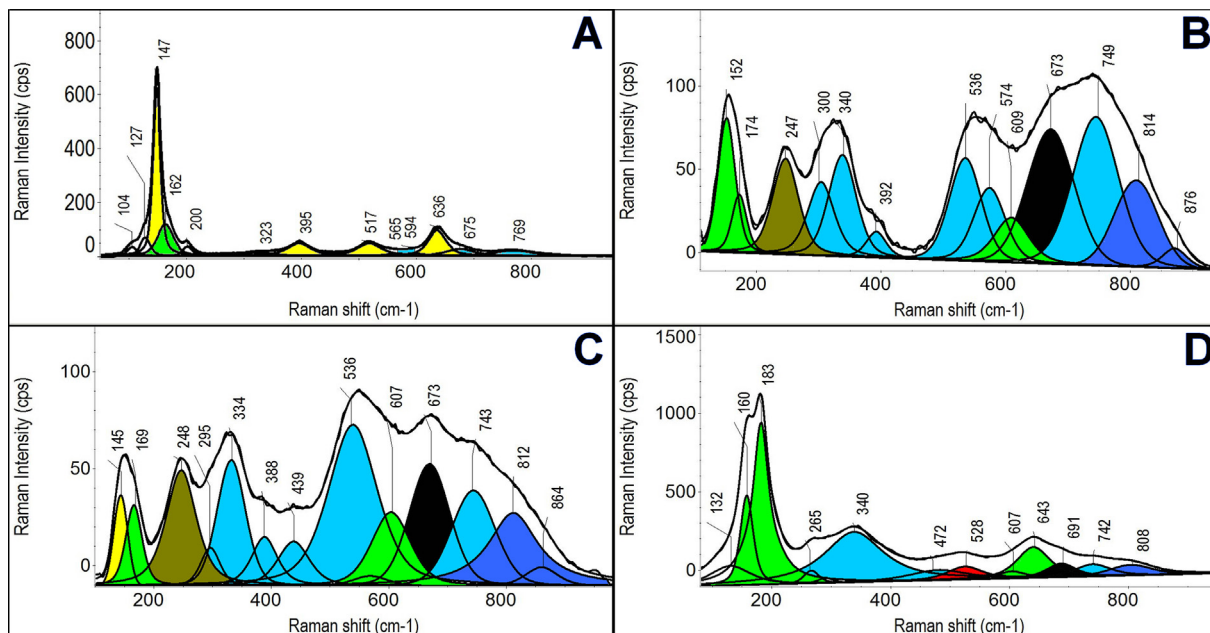


Fig. 6. Raman microspectra from points selected in the map of grains: A – (rim with a thickness of 3–4 μm) anatase, traces of brannerite and carbonaceous material; B – (layer 1–2 μm between the core and the outer grain layer) amorphous brannerite - UO_2^{2+} , uraninite; C – (grain core) anatase, amorphous brannerite - UO_2^{2+} , uraninite; D – (area to the north of the grain) highly crystalline brannerite with carbonaceous material. A list of spectral bands and their assignments is shown in Table 2.

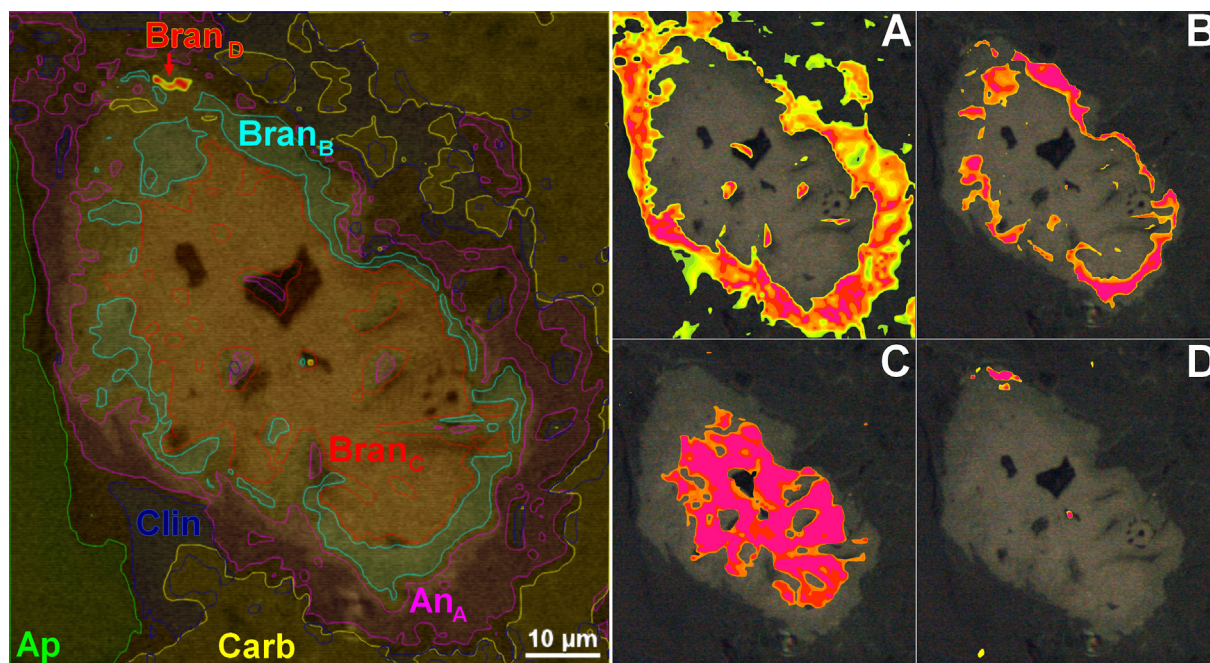


Fig. 7. Photomicrograph of the analyzed grain (left) with 2D correlation maps (A–D) of mineral phase distributions. Bran – brannerite, An – anatase, Ap – hydroxyapatite, Carb – carbonaceous matter. Subscripts refer to relevant maps and spectra. Maps A, B, C, and D correspond to the spectra in Fig. 6.

(Fig. 9 B and C). Their level varied from 20 to 60 vol% (Table 3). Particles up to 50 μm in size were commonly found in rocks, displaying metamorphic foliation (well-developed metamorphic structure), in which they formed 20–50 vol% of carbonaceous matter (samples ZCH-102 and ZCH-95). Particles larger than 50 μm (up to 200 μm) form up to 2 vol% in sample ZCH-31 and 23 vol% in sample ZCH-95. Particles greater than 50 μm in size were not detected in sample ZCH-102. Particles of Type II had average maximum reflectance R_{max} values from 3.58 vol% to 9.98 vol%, higher than Type I particles (Table 3), and they were variably anisotropic, from isotropic anthracite to optically

anisotropic graphite, which was accompanied by increased differences between R_{max} and R_{min} (bireflectance) (Taylor et al., 1998). Type II represents a mixture of carbonaceous particles of the anthracite to meta-anthracite transition stage, particularly in samples ZCH-8 and ZCH-102, particles of the semi-graphite transition stage, characterized by an R_{max} between 6 vol% and 9 vol% and crystalline graphite laminae with an R_{max} over 9 vol%, dominated in samples ZCH-94 and ZCH-95. They occurred separately (Fig. 9B and C) or formed aggregates (Fig. 9 D and E).

Type III represents dense rarely porous carbonaceous particles of

Table 2

List of Raman spectra bands, their assignment, and comparison with natural and synthetic brannerite data (Zhang et al., 2013).

| A | B | C | D | Natural brannerite Zhang et al., 2013 | Synthetic Ca _{0.2} U _{0.8} Fe _{0.2} Ti _{1.8} O ₆ | Assignment |
|----------|--------|--------|----------|--|---|--|
| hem | border | centre | north | | | |
| 147 | | 145 | | | | E _g anatas |
| | 152 | | 160 | 155 | | B _g ν ^{AS} (Ti-O) |
| 162 | 174 | 169 | 183 | 161 | 171–184 | B _g ν ^{AS} (Ti-O) |
| 200 | | | | | | E _g anatas |
| | 247 | 248 | | | | UO _{2.12} |
| | | | 265 | | 268 | A _g ν ^S (O-Ti-O) |
| | 300 | 295 | | 279 | | A _g ν ^S (O-Ti-O) |
| 323 | 340 | 334 | 340 | 391 | 328 | A _g ν ^S (O-Ti-O) |
| | 392 | 388 | | | | A _g ν ^S (O-Ti-O) |
| 395 | | | | | | B _g anatas |
| | | 439 | 528, 472 | | 432, 482 | ν(Fe-O) |
| 517 | | | | | | A _{1g} , B1g anatas |
| | 536 | 536 | | 530 | 533 | A _g ν ^S (O-Ti-O) |
| 565, 594 | 574 | | | | | A _g ν ^S (O-Ti-O) |
| | 609 | 607 | 643, 607 | 624 | 650 | B _g ν ^{AS} (Ti-O) |
| 636 | | | | | | E _g anatas |
| 675 | 673 | 673 | 691 | | 693 | ν(U-O) |
| | 749 | 743 | 742 | 743 s | 771 | A _g ν ^S (O-Ti-O) |
| | 814 | 812 | 803 | 824 | 832 | ν ₄ (U-O) UO ₂ ²⁺ |
| | 876 | 864 | | | | ν ₅ (U-O) UO ₂ ²⁺ |

irregular shape, with high-reflecting ($R_{max} = 3.34\text{--}7.15\%$), partly optically anisotropic, variable isometric or elongated particles of semi-graphite and solid bitumen (impsonite). They occurred in small veinlets (Fig. 9F) in altered rocks and in quartz veins, particularly in samples ZCH-10, ZCH-31 and ZCH-8, in which the lowest R_{max} values were found (Table 3).

The first-order Raman spectra of samples were dominated by two

prominent features similar to those of disordered carbonaceous matter. Carbonaceous material was found both in the anatase upper envelope of the analysed grain and in the surrounding matrix. The graphite lamellae of Type II in sample ZCH-95 with average maximum reflectance values R_{max} 9.98% (Table 3) showed the highest degree of graphitization. The Raman spectrum (Fig. 10, upper) of graphite particle with 9.65% R_{max} contained three intense sharp bands at 1350 (D1), 1581 (G) and 1623

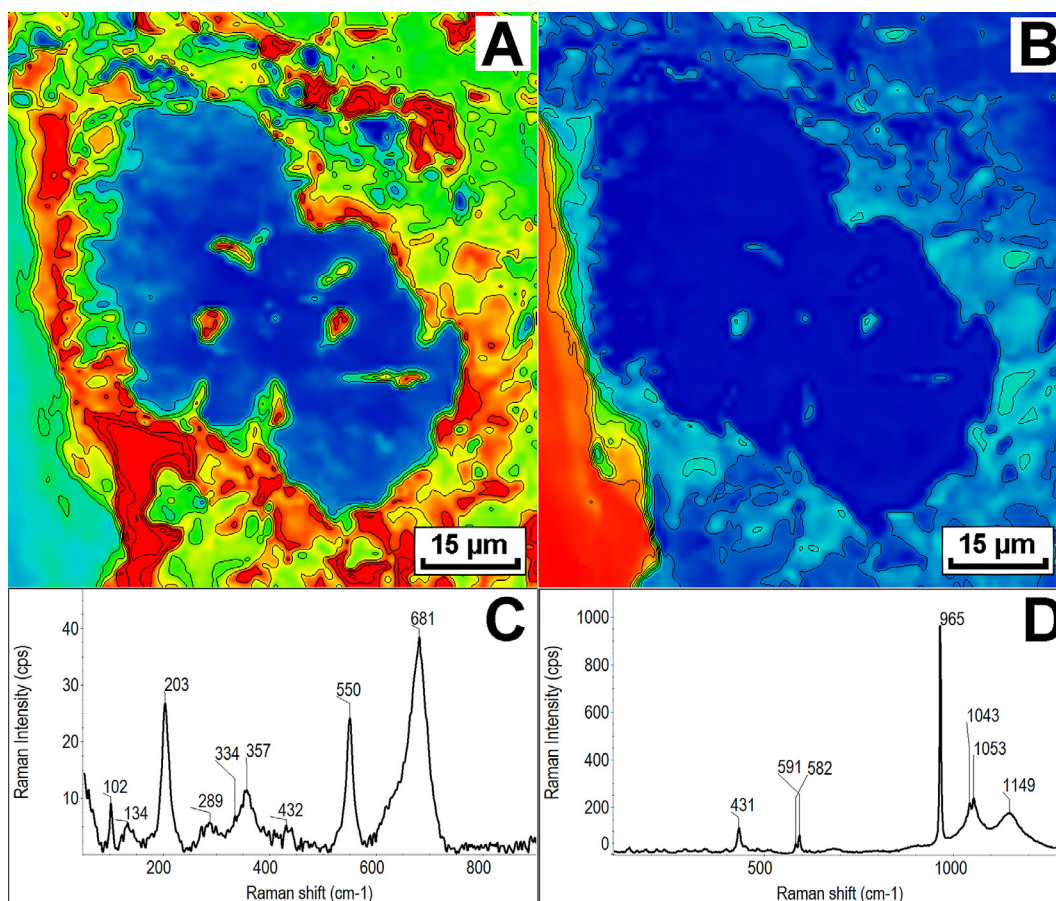


Fig. 8. 2D correlation maps and Raman spectra of chlorite (left) and hydroxyapatite (right) and their 2D correlation maps of occurrence in the grain.

Table 3

Random, maximum, and minimum reflectance values of carbonaceous particles and composition of their morphological types (R_r - random reflectance of all measured carbonaceous particles in normal light; σ - standard deviation; R_{\max} , R_{\min} - average values of maximum and minimum reflectance of three morphological types of carbonaceous particles measured in polarized light; X^* - reflectance values of solid bitumen measured in polarized light).

| Sample | R_r (%) | σ | Composition of morphological types (vol.%) | | | Reflectance of Type I | | Reflectance of Type II | | Reflectance of Type III | |
|---------|-----------|----------|--|---------|----------|-----------------------|----------------|------------------------|----------------|-------------------------|----------------|
| | | | Type I | Type II | Type III | R_{\max} (%) | R_{\min} (%) | R_{\max} (%) | R_{\min} (%) | R_{\max} (%) | R_{\min} (%) |
| ZCH-8 | 3.75 | 0.33 | 54.0 | 38.8 | 7.2 | 2.62 | 2.50 | 4.51 | 2.14 | 3.67 | 2.50 |
| ZCH-31 | 5.68 | 0.49 | 56.7 | 33.3 | 10.0 | 4.30 | 2.22 | 7.37 | 1.97 | 6.01 | 2.10 |
| ZCH-94 | 6.75 | 0.42 | 37.7 | 60.0 | 2.3 | 5.78 | 2.05 | 9.25 | 1.90 | 6.65 | 2.07 |
| ZCH-95 | 7.33 | 0.47 | 28.1 | 67.1 | 4.8 | 5.88 | 2.02 | 9.98 | 1.85 | 7.15 | 1.91 |
| ZCH-102 | 3.39 | 0.27 | 71.5 | 20.2 | *8.5 | 3.05 | 2.48 | 3.58 | 2.20 | *3.34 | *2.58 |

(D2) cm^{-1} . Band D2, related to disorder inside the graphite planes (E2g), cannot be distinguished in Raman spectra of substances with a lower degree of graphitization, and only a G band at $\sim 1600 \text{ cm}^{-1}$ was found in the spectrum of semi-graphite (sample ZCH-8, Fig. 10 bottom). Much larger values of FWHM-D1, which ranged from 100 to 260 cm^{-1} , were also apparent from the spectrum, over graphitic lamella with half-widths of about 42 cm^{-1} .

The typical structural parameters are shown in Table 4, where the components are ranked according to the increasing degree of graphitization, expressed on the decreasing half-widths of the strip D1 (FWHM-D1), which is a suitable structural parameter for evaluating coal (Sýkorová et al., 2016; Hinrichs et al., 2014). The lowest degree of graphitization exhibited a carbonaceous matter that was dispersed in the anatase envelope of brannerite/uraninite grains and had an FWHM-D1 of 260 cm^{-1} . A slightly lower average value was also exhibited by carbonaceous matter that was unevenly distributed around the grain as seen from the 2D distribution correlation map of the graphite material (Fig. 11).

4.6. Organic extract analysis

The samples contained 0.0001–0.02% of extractable matter that corresponded with the low total organic carbon and hydrogen contents (Table 5).

In the extracts, *n*-alkanes were the main constituents, ranging from *n*-C₁₆ to *n*-C₂₇ (Fig. 12), and two types of *n*-alkane distribution were distinguished. The first type showed dominant long-chain *n*-alkanes with a maxima at *n*-C₂₄₋₂₆, and the second type with predominantly middle-chain *n*-alkanes with a maxima at *n*-C₂₁ (Fig. 13). Except for sample ZCH95, all extracts revealed a secondary maximum at *n*-C₁₈ within the distribution for short-chain *n*-alkanes. Alkenes and acyclic isoprenoids, including pristane (Pr), phytane (Ph), and squalene, fatty acids and their esters, and diterpenoids including fichtelite (18-norabietane), 18-norabietane-8,11,13-triene, totarol (14-isopropylpodocarpa-8,11,13-trien-13-diol) and retene, were also identified in the extracts (Table 6).

5. Discussion

5.1. Origin of mineralised shear zones and temperatures of hydrothermal alteration

The origin of shear zones is compatible with N–S dextral kinematics. These zones of brittle deformation are associated with phyllosilicate- and organic matter-rich coherent and incoherent cataclastites and fault breccias, from 30 cm to approximately 1–2.5 m in thickness.

The pre-ore stage was characterised by widespread chloritisation, argillisation, and hematitisation of highly metamorphosed sediments. In comparison to the French deposits (Poty et al., 1986), the altered high-grade metasediments from the western part of the Bohemian Massif (Zadní Chodov, Wäldel/Mähring, e.g., Dill 1985, 1986) are characterised by higher activities of Mg-rich solutions and by younger

carbonatisation. The lower Fe/Fe + Mg ratio of chlorites from uranium deposits in the western part of the Bohemian Massif (this paper and Hecht et al., 1991), when compared to the Massif Central (e.g., Cathelineau, 1986), is related to higher activity of the Mg-rich fluids in the study area. According to Dill (1986), the sources of Mg can be traced back to carbonates and calcium-silicate rocks of the Moldanubian Zone.

The temperature of the ore stage could be estimated from chlorite thermometry, applied to chlorite II, yielding a range from 122 °C to 258 °C. Similar temperatures were found for uranium mineralisation at the Hebanz uranium deposit, occurring in the Fichtelgebirge pluton (Hecht et al., 1991). Temperatures in the post-ore quartz stage, estimated from fluid-inclusion thermometry in the Zadní Chodov and Vítkov II uranium deposits in the Bor pluton, suggest that significant temperature fluctuations, from 66 °C to 260 °C, occurred during the post-ore stage (Topp, 1993).

5.2. Brannerite

The occurrence of brannerite in the Zadní Chodov uranium deposit and related uranium deposits in the Bor pluton area were significant (René and Dolníček, 2017). Brannerite is not found in other Variscan uranium deposits in the Bohemian Massif, nor in similar vein-type ore deposits in France. Brannerite has been found in acite-hosted uranium deposits in the Mount Isa uranium district, Queensland, Australia (Polito et al., 2009; Wilde et al., 2013), and similar uranium occurrences have been reported in Aricheng South, Guyana (Alexandre, 2010), in giant iron-oxide copper-gold-silver uranium deposits at Olympic Dam, South Australia (Macmillan et al., 2017), and in the metasomatised metasedimentary rock series of the Central Ukrainian uranium province (Cuney et al., 2012).

The chemical composition of brannerite is nominally UTi_2O_6 . However, in brannerite from the hydrothermal uranium deposits, uranium may be replaced by Ca, Th, Y and REE, while Si, Al and Fe can replace titanium as a result of oxidation and partial hydration (Smith, 1984). The presence of Pb in its structure is mainly due to the decay of U. Brannerites from metasomatic uranium deposits of the Central Ukrainian uranium province are enriched in Si and Ca (Cuney et al., 2012). The unaltered brannerite from the Zadní Chodov uranium deposit, in comparison to brannerite from the uranium deposits in Australia and Guyana, was depleted in Si and Al. Uranium in the ideal brannerite is tetravalent $\text{U}^{4+}\text{Ti}_2\text{O}_6$, while it is partially oxidized to the hexavalent cation UO_2^{2+} in natural brannerite.

Raman spectroscopic studies of brannerite are very rare and were performed only on samples from the Olympic Dam uranium deposit and/or brannerite from granitic pegmatite (Sierra Albarrana region, southern Spain) (Frost and Reddy, 2011; Charalambous et al., 2012; Zhang et al., 2013).

In this study, three structural layers were distinguished in the grains of brannerite and were not separate mineral phases, but mixtures of anatase, carbonaceous matter and brannerite itself. Towards the inside of the grain, brannerite was more amorphous and was partly oxidized,

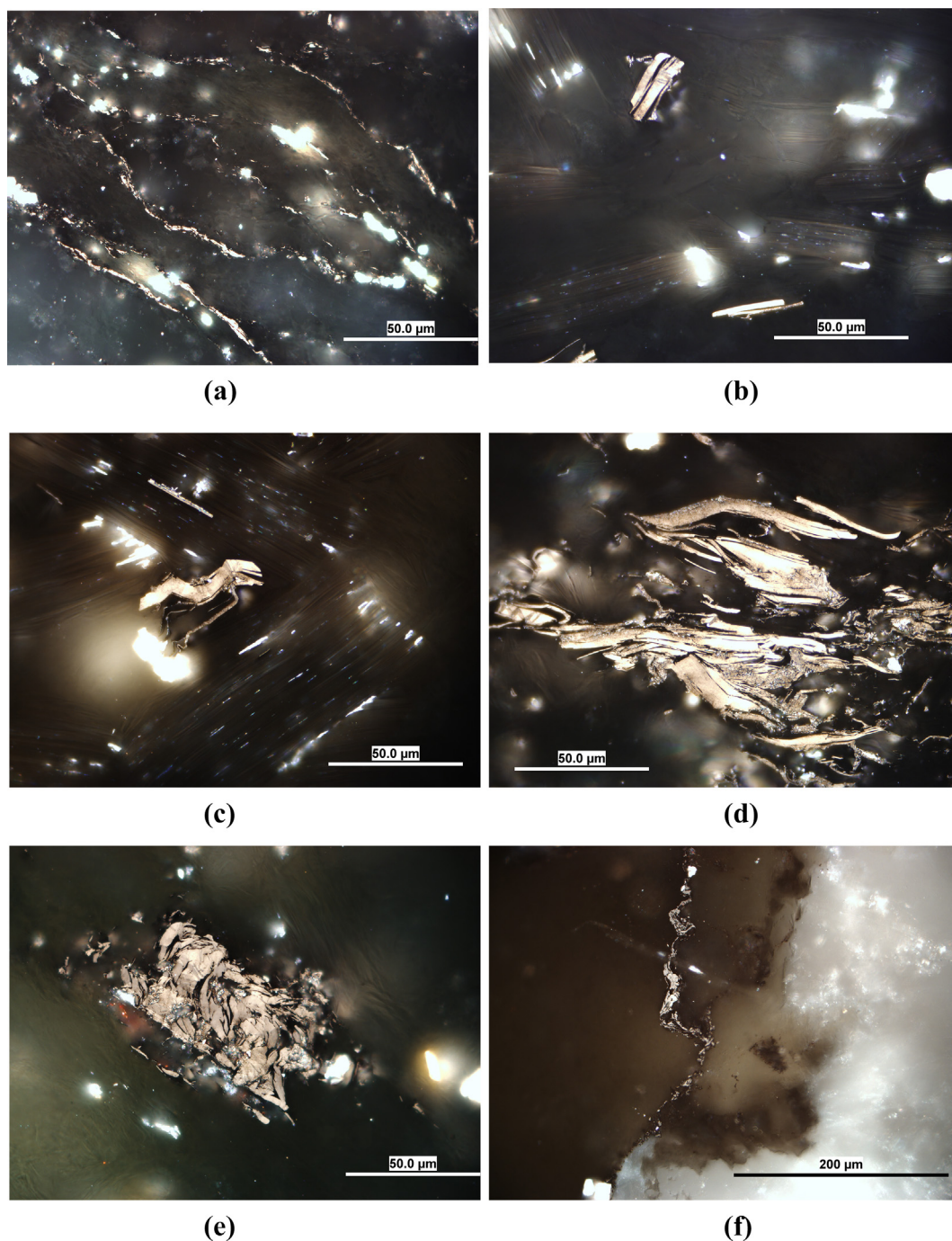


Fig. 9. Reflected light photomicrographs, showing characteristic types of dispersed carbonaceous matter from sediments in Zadní Chodov (oil immersion, polarized light). A: Type I particles with lines of fine-grained elongated particles (sample ZCH-31). B: Type II particles with lath-shaped carbonaceous matter (sample ZCH-95). C: Type II particles with lath-shaped anisotropic carbonaceous particle (graphite) (sample ZCH-95). D: A cluster of large lamellar semi-graphitic and graphitic particles of Type II (sample ZCH-94). E: Aggregate of mineralised and porous matter of lath-shaped particles Type II and Type III, formed by dense particles of meta-anthracite stage (sample ZCH-31). F: Irregular filling of a crack in the mineral phase with solid bitumen (imponite) (sample ZCH-102).

containing UO_2^{2+} . The specific band at 247 cm^{-1} indicates non-stoichiometric uranium oxide $\text{UO}_{2.12}$ (Manara and Renker, 2003). The matrix around the grain (and partly inside of it) was composed of chlorite, hydroxyapatite, and carbonaceous matter. Pyrite and brookite were detected only locally.

Low Pb contents and presence of uraninite in the grain core, or between the core and the outer grain layer, imply later deposition of brannerite. It could be a product of a later uranium mineralizing event or may have been precipitated during a later-stage hydrothermal uranium event that involved dissolution with reprecipitation of already

precipitated uraninite.

5.3. Composition and origin of the carbonaceous matter

Previous studies suggested that carbonaceous matter is generally more sensitive to tectonic shear strain than clay minerals (Robert, 1988; Árkai et al., 2002; Suchý et al., 2007). It should be remembered that clay minerals and inorganic components in general are involved in the graphitization of carbonaceous substances, as summarized by Rodrigues et al. (2012). In the experimental multi-stage and high-

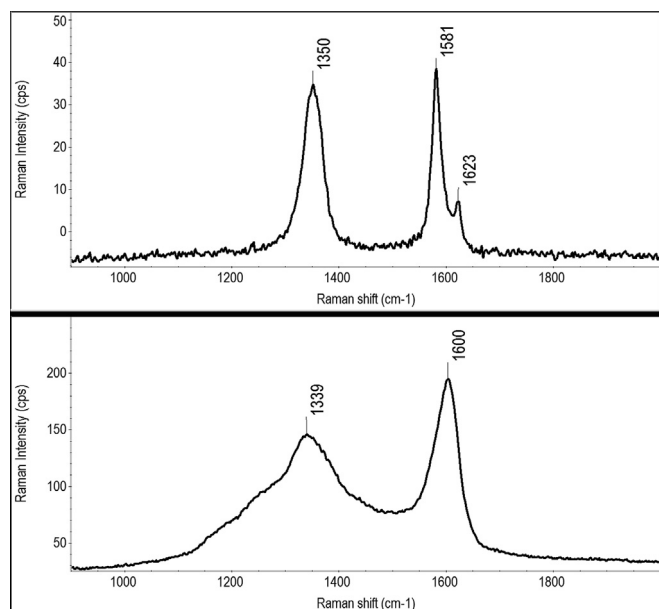


Fig. 10. Raman spectra of graphite lamella (top) of sample ZCH-95, and carbonaceous particle with lower graphitization (bottom) of ZCH-8 (structural parameters are in Table 4).

temperature graphitization of anthracites up to 2500° C, catalytic effects of the mineral matter were found. Not only the content, type and distribution of minerals in the original materials but also the newly formed mineral phases, such as carbides with such elements as Fe, Al, K, Si, Ti, can enhance the graphitization of anthracites (Rodrigues et al., 2012). The optical microscopic investigation of altered high-grade metasediments and infills of samples showed a mixture of various types of dispersed carbonaceous matter with contrasting optical reflectance values and limited solubility in organic solvents that reveal varying thermal transformation. Highly matured, semi-graphitic and graphitic particles coexisted, being mixed within the samples. Fine-grained carbonaceous particles of Type I dominated in samples ZCH-8, ZCH-31 and ZCH-102 showed somewhat lower reflectance values and a degree of structural ordering that correspond to the anthracite and meta-anthracite stage, according to Kwiecińska and Petersen (2004). These Type I particles represent original carbonaceous matter, dispersed in the meta-sediments, and prevail in samples with preserved sedimentary structures.

Type II carbonaceous particles, abundant in samples ZCH-94 and ZCH-95, consisted of two populations. The first population (R_{max} less than 9 vol%; Table 3) corresponded to the meta-anthracite and semi-graphite stages described by Kwiecińska and Petersen (2004). Optically similar, very thermally mature carbonaceous materials have been described as “transitional matter” (Diessel and Öffler, 1975), “poorly ordered graphite” (Křibek et al., 1994) or “material of transitional phase” in the stage of coalification – graphitisation (Kwiecińska and Petersen,

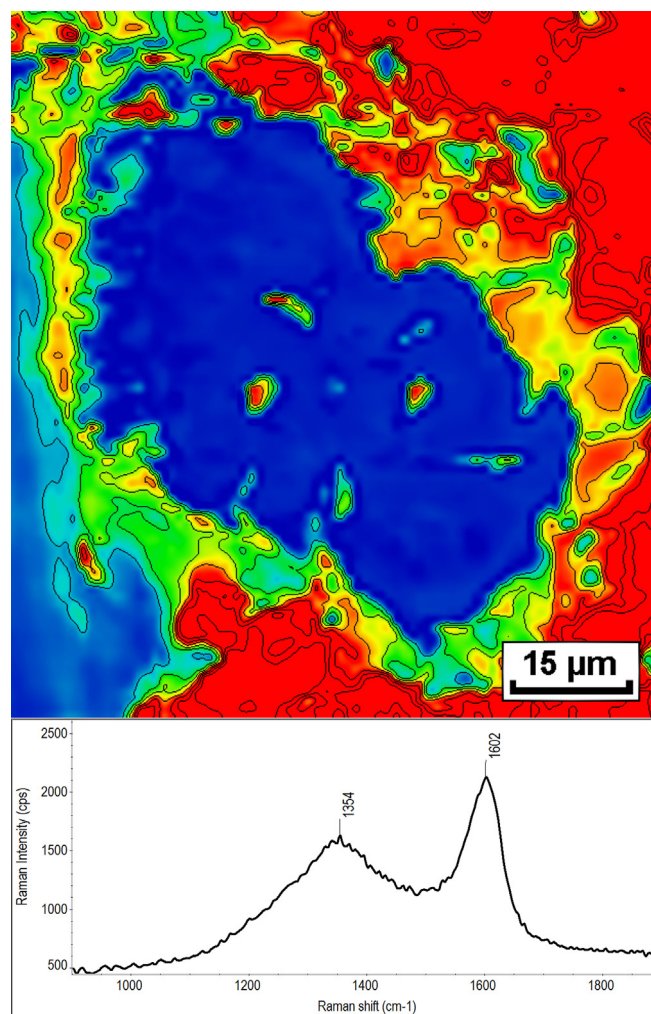


Fig. 11. Distribution 2D correlation map of graphitic material and its Raman spectrum.

Table 5

Total carbon content, total organic carbon content, hydrogen content, uranium content in bulk samples, pristane/phytane (Pr/Ph) ratio, pristane to n -C₁₇ alkane (Pr/ n -C₁₇) and phytane to n -C₁₈ alkane (Ph/ n -C₁₈) ratios. ^d – dry basis; _t – total.

| | C _t ^d wt% | TOC wt% | H ^d wt% | U ppm | Pr/Ph | Pr/ n -C ₁₇ | Ph/ n -C ₁₈ |
|--------|------------------------------------|------------|-----------------------|----------|-------|--------------------------|--------------------------|
| ZCH8 | 0.17 | 0.15 | 1.55 | 1290 | 0.06 | 0.14 | 0.45 |
| ZCH31 | 0.17 | 0.14 | 0.79 | 22 | 0.16 | 0.17 | 0.39 |
| ZCH94 | 0.77 | 0.57 | 1.43 | 735 | 0.40 | 0.31 | 0.52 |
| ZCH95 | 3.91 | 0.86 | 1.23 | 77 | 0.13 | 0.34 | 0.55 |
| ZCH102 | 1.62 | 1.14 | 1.12 | 25 | 0.30 | 0.54 | 0.33 |

Table 4

Structural parameters obtained by Raman spectroscopy: $R_1 = I_{D1}/I_G$, $R_2 = A_{D1}/(A_{D1} + A_G + A_{D2})$, where I and A are intensities and areas of respective bands).

| Sample | D ₁ position cm ⁻¹ | FWHM-D ₁ cm ⁻¹ | G position cm ⁻¹ | FWHM-G cm ⁻¹ | R ₁ | R ₂ |
|----------------------------|---|---|--------------------------------|----------------------------|----------------|----------------|
| ZCH8 graphite in anatase | 1358 | 260 | 1587 | 104 | 0.920 | 0.690 |
| ZCH8 grain surrounding | 1353 | 257 | 1598 | 75 | 0.755 | 0.721 |
| ZCH8 graphite | 1340 | 244 | 1599 | 56 | 0.611 | 0.638 |
| ZCH8 graphite fine-grained | 1338 | 240 | 1601 | 51 | 0.639 | 0.630 |
| ZCH8 graphite in brookite | 1350 | 209 | 1598 | 69 | 0.650 | 0.559 |
| ZCH8 brannerite (north) | 1365 | 195 | 1599 | 86 | 0.850 | 0.640 |
| ZCH8 graphitic lamellae | 1348 | 100 | 1585 | 53 | 1.310 | 0.710 |
| ZCH95 graphitic lamellae | 1350 | 42 | 1581 | 21 | 0.990 | 0.657 |

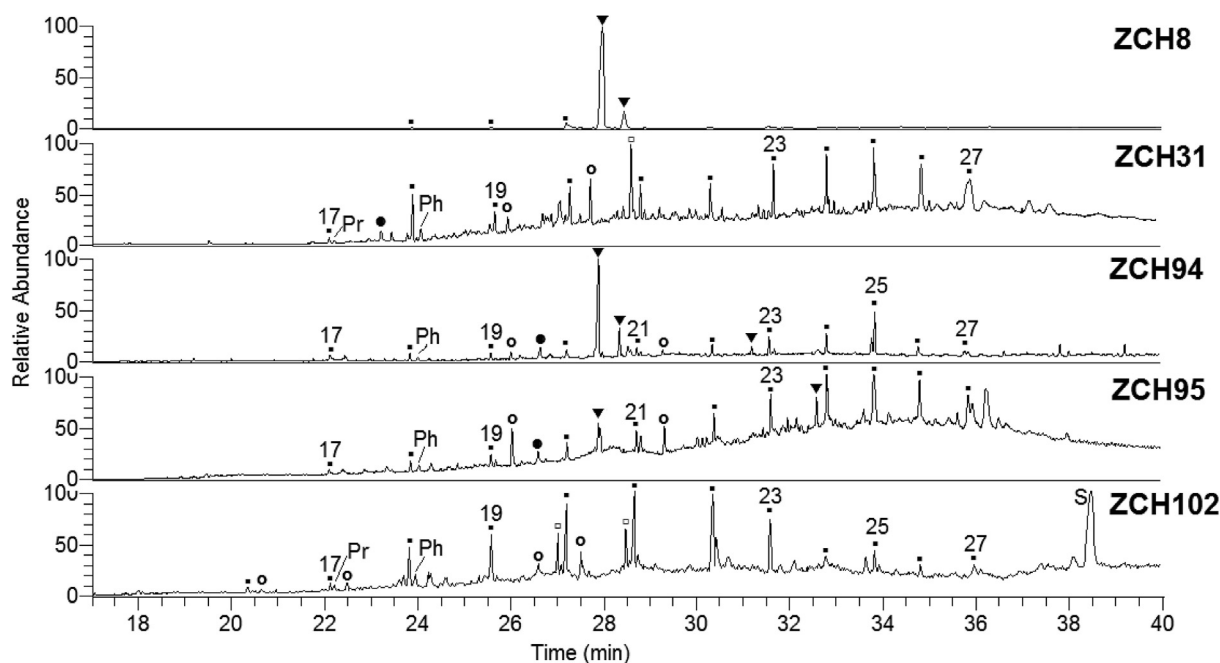


Fig. 12. Total ion chromatograms of the sediment extracts. The identified compounds are listed in Table 6: ■ = *n*-alkanes, □ = alkenes, ○ = fatty acid esters, ▼ = terpenoids, ● = fatty acids, Pr = pristane, Ph = phytane, S = squalene.

2004). The present results show that Type II particles were formed either *in situ* by solid state transformation of Type I particles or by crystallization from metamorphic fluids according to Wopenka and Pasteris (1993). They distinguished syngenetic graphite formed through the metamorphic evolution of carbonaceous matter dispersed in the sediments and epigenetic graphite, originating from precipitation of solid carbon from carbon-saturated C–H–O fluids.

The second population of Type II particles represents crystalline material with strong optical anisotropy and the highest degree of graphitization, according to Raman spectroscopic parameters. Similar carbonaceous matter as Type II from the Zadní Chodov ore deposit was described by Křibek (1981, 1989) and Křibek et al. (2009) from the Rožná and Dyleň uranium deposits. However, they found a low degree of graphite crystallinity in these deposits that can be explained by its oxidation during hydrothermal processes: oxidation leads to destruction of the graphite, i.e., a gradual splitting off of graphite lamellae,

reflected in a decrease in its crystallinity (Volkenstein, 1960; Rudorff et al., 1963; Pauling, 1966).

Optically and morphologically similar carbonaceous matter as Type II particles were also described by Suchý et al. (2007) in the Neoproterozoic shales of the Teplá-Barrandian Zone, by Křibek et al. (2008) in Paleoproterozoic black shales of the Kaya-Goren greenstone belt (Burkina Faso), and by Křibek et al. (2015) in Paleoproterozoic gold deposits in West Africa. Ziegenbein et al. (1989) found that the metasediments from the KTB borehole in Bavaria (Germany) contained two types of graphites: finely distributed graphite in paragneisses and obvious enrichment of graphite in fault zones. Occurrence and crystallinity of this graphite occurrence was extensively discussed (e.g., Walther and Althaus, 1988; Ziegenbein and Johannes, 1990; Reutel, 1992; Dill et al., 2019), and it was concluded that graphite accumulations in shear zones evolved in high-grade metasediments, originating from accumulations of carbon from the gas phase, according to the

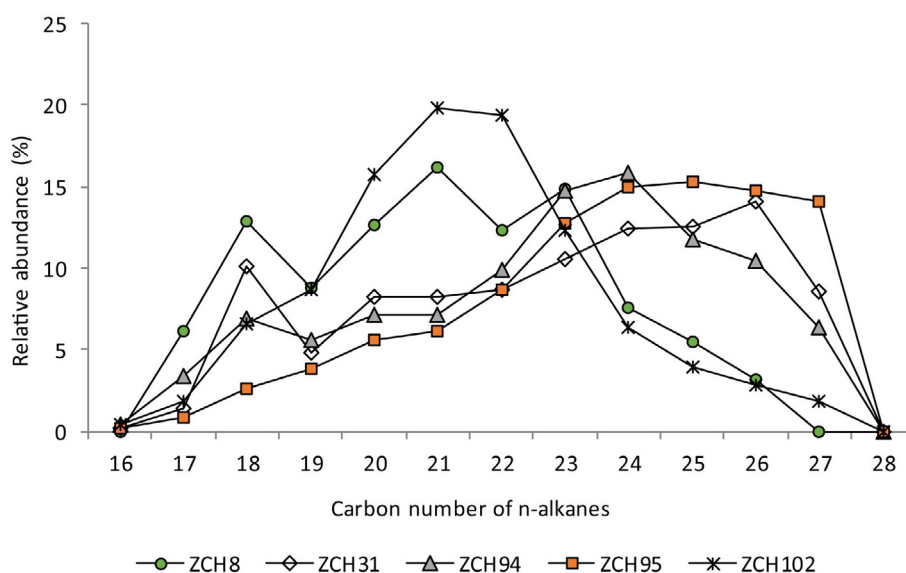


Fig. 13. The relative *n*-alkane distributions within sample extracts (using selected ion monitoring m/z 85).

Table 6
The compounds identified in the sample extracts.

| | RT (min) | Compound | MW | Formula | Relative abundances (%) | | | | | | |
|----|-------------|--|-----|--|-------------------------|-------|-------|-------|-------|-------|---------|
| | | | | | ZCH6 | ZCH8 | ZCH25 | ZCH40 | ZCH94 | ZCH95 | ZCH102A |
| ■ | 20.3 | <i>n</i> -C ₁₆ alkane | 226 | C ₁₆ H ₃₄ | 5.7 | 8.0 | 1.4 | 1.3 | 1.6 | 1.2 | |
| ○ | 20.5 | dodecanoic acid, 1-methylethyl ester | 242 | C ₁₅ H ₃₀ O ₂ | | 2.6 | | | | 0.5 | |
| ■ | 22.2 | <i>n</i> -C ₁₇ alkane | 240 | C ₁₇ H ₃₆ | 5.1 | 6.8 | 25.6 | 9.8 | 10.0 | 5.7 | 5.6 |
| Pr | 22.2 | pristane | 268 | C ₁₉ H ₄₀ | 3.7 | 0.9 | 3.9 | 2.9 | 0.7 | 7.2 | 2.1 |
| ○ | 22.6 | benzoic acid, 2-ethylhexyl ester | 234 | C ₁₅ H ₂₂ O ₂ | | | 13.3 | | | | 3.7 |
| ● | 23.2 | tetradecanoic acid | 228 | C ₁₄ H ₂₈ O ₂ | | | | 12.6 | | | |
| ■ | 23.8 | <i>n</i> -C ₁₈ alkane | 254 | C ₁₈ H ₃₈ | 17.2 | 14.8 | 49.3 | 70.6 | 20.3 | 17.5 | 19.8 |
| Ph | 23.9 | phytane | 282 | C ₂₀ H ₄₂ | 7.7 | 6.6 | 10.8 | 12.8 | 3.8 | 13.0 | 6.5 |
| □ | 25.2 | C ₁₉ alkene | 242 | C ₁₆ H ₃₄ O | | | 79.3 | | | | |
| ■ | 25.6 | <i>n</i> -C ₁₉ alkane | 268 | C ₁₉ H ₄₀ | 25.3 | 10.3 | 43.4 | 33.5 | 16.3 | 25.1 | 25.8 |
| ○ | 25.8 | hexadecanoic acid, methyl ester | 270 | C ₁₇ H ₃₄ O ₂ | 83.5 | | 4.6 | 27.9 | 15.8 | 71.3 | 2.4 |
| ● | 26.3 | hexadecanoic acid | 256 | C ₁₆ H ₃₂ O ₂ | 62.1 | | | | 19.3 | 27.4 | |
| □ | 27.0 | C ₂₀ alkene | 280 | C ₂₀ H ₄₀ | | | | | | | 24.1 |
| ■ | 27.1 | <i>n</i> -C ₂₀ alkane | 282 | C ₂₀ H ₄₂ | 34.5 | 14.7 | 72.8 | 57.4 | 20.9 | 36.2 | 46.8 |
| ○ | 27.5 | hexadecanoic acid, 1-methylethyl ester | 298 | C ₁₉ H ₃₈ O ₂ | 85.1 | | | 62.9 | | | 15.5 |
| ▼ | 27.9 | fichtelite (18-norabietane) | 262 | C ₁₉ H ₃₄ | | 100.0 | | | 100.0 | 38.0 | |
| □ | 28.3 | C ₂₁ alkene | 294 | C ₂₁ H ₄₂ | 62.1 | | | 100.0 | | | |
| ▼ | 28.4 | 18-norabieta-8,11,13-triene | 256 | C ₁₉ H ₂₈ | | 11.8 | | | 22.3 | | |
| ■ | 28.7 | <i>n</i> -C ₂₁ alkane | 296 | C ₂₁ H ₄₄ | 41.4 | 18.9 | 100.0 | 57.7 | 20.7 | 40.5 | 59.0 |
| ○ | 28.8 | octadecenoic acid, methyl ester | 294 | C ₁₉ H ₃₄ O ₂ | 46.0 | | | | | | |
| ○ | 29.1 | octadecanoic acid, methyl ester | 298 | C ₁₉ H ₃₈ O ₂ | 58.4 | | | | 22.1 | 22.8 | |
| ■ | 30.4 | <i>n</i> -C ₂₂ alkane | 310 | C ₂₂ H ₄₆ | 58.6 | 10.7 | 75.4 | 60.9 | 28.8 | 56.4 | 57.8 |
| ▼ | 31.2 | retene | 234 | C ₁₈ H ₁₈ | | | | | 13.2 | | |
| ■ | 31.4 | <i>n</i> -C ₂₃ alkane | 324 | C ₂₃ H ₄₈ | 72.4 | 14.1 | 43.1 | 73.8 | 43.0 | 83.1 | 36.7 |
| ▼ | 32.6 | totarol | 236 | C ₂₀ H ₃₀ O | | | | | | 54.0 | |
| ■ | 32.8 | <i>n</i> -C ₂₄ alkane | 338 | C ₂₄ H ₅₀ | 86.2 | 8.7 | 24.0 | 87.2 | 46.2 | 98.0 | 19.1 |
| ■ | 33.9 | <i>n</i> -C ₂₅ alkane | 352 | C ₂₅ H ₅₂ | 86.2 | 6.2 | 15.3 | 87.3 | 34.2 | 100.0 | 11.8 |
| ■ | 34.7 | <i>n</i> -C ₂₆ alkane | 366 | C ₂₆ H ₅₄ | 94.3 | 3.4 | 10.2 | 98.3 | 30.6 | 96.5 | 8.4 |
| ■ | 35.9 | <i>n</i> -C ₂₇ alkane | 380 | C ₂₇ H ₅₆ | 100.0 | | 5.8 | 60.1 | 18.7 | 90.3 | 5.6 |
| S | 38.3 | squalene | 410 | C ₃₀ H ₅₀ | | | 91.0 | | | | 100.0 |

Peaks were quantified in the TIC mode. Relative abundance normalised to major compound peak = 100.

MW = Molecular Weight.

RT = Retention Time.

reaction: $\text{CO}_2 + \text{CH}_4 \rightarrow 2\text{C} + \text{H}_2\text{O}$. This reaction was confirmed by fluid inclusion studies (Reutel, 1992; Topp, 1993). Heterogeneous assemblages of several types of carbonaceous matter with contrasting thermal maturity were found in the Neoproterozoic samples from the Teplá-Barrandian Zone, and these were similar to those of prehnite-pumpellyite- and greenschist-facies metamorphic rocks elsewhere (Diessel and Öffler, 1975; Křibek et al., 1994; Suchý et al., 2007). An important catalytic factor in enabling the process of graphitisation, oriented tectonic pressure was found in many very low- and low-grade metamorphic rocks (Diessel and Öffler, 1975; Diessel et al., 1978; Suchý et al., 1997). According to Diessel and Öffler (1975), graphitisation begins within the chlorite zone of the greenschist facies and is complete before the beginning of the amphibolite facies at temperatures from 380° to 450 °C and pressures between 2×10^8 Pa and 3×10^8 Pa. Graphite was also recognised in some high-grade metasediments from the Teplá-Barrandian Zone and interpreted in terms of allochthonous detrital components (Jehlička and Rouzaud, 1990; Jehlička and Bény, 1992). Suchý et al. (2007) assumed that most graphite particles in these Neoproterozoic sediments are actually newly formed autochthonous components rather than detrital fragments. Strongly graphitised particles are characteristically elongated, sub-parallel to cleavage plains and along grain boundaries of flattened quartz, or are dynamically recrystallised ribbon quartz grains.

Type III particles resemble dense particles of anthracite to semi-graphite stages, and dense fragments of pyrobitumen (impsonite) (Jacob, 1989), and according to Kwecińska and Petersen (2004), carbonaceous matter of anthracite stage. They are products of hydrocarbon (migrabitumens) migration during the hydrothermal alteration of the rock complex. Similar carbonaceous matter was also found by Dill and Weiser (1981) near the Wäldel/Mähring uranium deposit in Bavaria (Germany) and also described as impsonite. Also Dill et al. (2019) deals

with age, origin and composition of impsonite in connection with conditions of origin and properties of graphite and semi-graphite along the western edge of the Bohemian Massif. According to Křibek et al. (2015), the carbonaceous matter, precipitated from C–O–H fluids, has been attributed to carbon supersaturation as a result of several principal processes: (1) cooling of the hydrothermal fluids, (2) fluid compositional changes, and (3) the infiltration of oxidized C–O–H fluids into a reduced environment. Optical properties and structural ordering of carbonaceous matter depend mostly on temperature. At the experimental graphitization of anthracite at temperatures over 1500 °C and with increasing temperatures, other graphitic structures were developed, such as crystalline aggregates, flakes, and microspheres (Rodrigues et al., 2011). The effect of pressure is much smaller, being manifested mainly in metamorphic rocks or faults when, due to oriented pressure, an increase in reflectivity and better structural ordering of carbonaceous matter particles may occur (Wada et al., 1994; Oohashi et al., 2011).

The Bohemian Massif is not the only host of stratiform deposits, but it also comprises vein-type organic matter accumulations such as graphite and solid bitumen derivatives of radiolytic polymerization of gaseous and liquid hydrocarbons (Dill, 1983; Křibek et al., 1999, 2009; René, 2017).

The relationship between the carbonaceous matter of the Zadní Chodov and Dyleň uranium deposits and graphite, evolved in graphite deposits of the Moldanubian Zone (Český Krumlov and Týn nad Vltavou areas), was documented by virtually identical isotopic composition of both types of carbonaceous substances (Kropotova et al., 1976; Křibek, 1981). The examined values ($\delta^{13}\text{C}$, PDB = -19.5 and -20.8 for carbonaceous matter from the Zadní Chodov deposit) do not differ from the isotopic composition of carbonaceous matter derived from biological sources (Hoefs, 1997).

Structural parameters of the graphitic material were not dependent in any way on the distance from uranium minerals, and it can be concluded that no radiation-based alteration of organic matter occurred, as was found in the case of radiation alteration of coal with coffinite and the generation of haloes (Sýkorová et al., 2016).

5.4. Composition and origin of organic substances

Due to the age of the basic original samples, deep burial and leakage, thermal transformation (temperature reached up to 260 °C during the *syn*-ore and post-ore stages), and the environment (with migration and interactions of hydrothermal fluids), any preservation of significant original biological traces is most unlikely; the cyanobacterial fossil record is among the oldest for any group of organisms, and hopane derivatives are their remnants in the sediments (Peters et al., 2005). These biomarkers were not documented in the samples studied here, and alkylalkanes or alkylcycloalkanes that are also associated with cyanobacteria and with Precambrian rocks were not observed.

The observed distribution of *n*-alkanes having mainly middle and higher molecular weight homologues (greater than 21) and no odd-to-even carbon number predominance (Fig. 13) was not specific. This is different from the typical *n*-alkane distribution of Proterozoic sediments with higher abundances of low molecular weight *n*-alkanes (Pawlowska et al., 2013; Flannery and George, 2014; Luo et al., 2015). Together with the identified diterpenoids and fatty acids, the *n*-alkanes originate from plant-released compounds because short-chain *n*-alkanes (< *n*-C₂₀) are usually considered to be derived from cyanobacteria, algae or other microorganisms, mid-chain *n*-alkanes from aquatic plants and the higher *n*-alkanes (> *n*-C₂₅) from waxes of terrestrial higher plants (Peters et al., 2005; Wang et al., 2010).

Also, presence of the isoprenoid compounds pristane (Pr) and phytane (Ph) confirms a biogenic source as they are products of geological alteration of phytol or other natural products (Peters et al., 2005). The Pr/Ph ratio, commonly used as a correlation parameter, was very low (Table 5), indicating saline and hypersaline conditions during mineral deposition. Values of salinity, under which the formation of mineralization occurred in uranium deposits, ranged from 20 to 30 wt% NaCl (Cuney et al., 2003). Squalene, a C₃₀ acyclic isoprenoid, is a major lipid, produced by archaea, but was also identified in alkaliphilic bacteria, grown at an extremely alkaline pH (10.5) and high salinity (2–4 M of total Na⁺), and so its occurrence can be attributed to extreme and harsh environments like hot springs, salt lakes, and marshlands (Banciu and Muntyan, 2015). The Pr/*n*-C₁₇ and Ph/*n*-C₁₈ ratios (Table 5), diagnostic parameters for depositional environments and organic matter maturation (Peters et al., 2005), show that matter was non-biodegraded and thermally matured.

Fatty acids in their free state are degraded rapidly in both oxic and anoxic depositional systems, hence they could not contribute significantly to sedimentary organic matter (Sun et al., 1997). However, fatty acid methyl esters can be preserved in a later stage of catagenesis than free fatty acids. Nevertheless, their presence in the extracts is indicative of an input of younger material and low degradation of organic matter. This agrees with the presence of diterpenoids that are products of plants, particularly of conifers: totarol, fichtelite, 18-norabieta-8,11,13-triene, retene. Fichtelite and 18-norabieta-8,11,13-triene also provide evidence about the occurrence of reductive processes during the deposition of organic matter (Otto and Simoneit, 2002).

To summarize, the results of the sample extract analyses show biomarkers that are younger and not related to the accumulation of organic matter in the pre-ore, *syn*-ore, and post-ore stages. They seem to be of gymnosperm source. Although gymnosperms have occurred since the Permian, the identified compounds are typical for Tertiary and younger sediments. The presence of uranium minerals did not have any effect on the biomarkers identified, but generally, according to the diagnostic parameters, mineralization setting did have an effect on biomarker status.

6. Conclusions

Mineralisation is a process with impact on organic material in sediments, and sedimentary organic matter is a sensitive marker for environmental and alteration processes. Results of the study of samples from uranium ore-enriched shear zones of the Zadní Chodov uranium deposit revealed:

- Evidence of higher activity of Mg-rich fluids in the study area during *syn*-ore stage, with temperatures from 122 °C to 258 °C, and the presence of coffinite and brannerite minerals;
- Structural differences within grains of brannerite and in the surrounding matrix;
- Evidence of original organic matter dispersed in the meta-sediments that were accompanied to the shear zones;
- Presence of meta-anthracite and semi-graphite particles formed either *in situ* by solid state transformation of original organic matter or by crystallization from metamorphic fluids;
- Presence of crystalline material with a high degree of graphitization, clusters of carbonaceous particles, and fragments of pyrobitumen (impsonite) as products of hydrocarbon migration in the hydrothermal fluids;
- Evidence of partial oxidation during hydrothermal processes due to the presence of brannerite containing UO₂²⁺ together with preserved large graphite lamellae;
- Identified organic biomarkers in the extractable fraction were of a younger age with low thermal maturity and the presence of typical Tertiary signatures.

Declaration of Competing Interest

The authors declare that they have no known competing financial interests or personal relationships that could have appeared to influence the work reported in this paper.

Acknowledgements

This study was supported by the Czech Science Foundation grant 19-05360S “Radiolytic alteration of organic matter in uraniumiferous environment”. Our thanks are to the Operational Program Prague - Competitiveness, project “Centre for Texture Analysis” (No. CZ.2.16/3.1.00/21538), and the long-term conceptual development of the research organization RVO: 67985891. Geological Institute, Academy of Sciences of the Czech Republic, is thanked for the interpretation of X-ray diffraction analysis and for performing the microprobe analyses.

Appendix A. Supplementary data

Supplementary data to this article can be found online at <https://doi.org/10.1016/j.oregeorev.2020.103428>.

References

- Alexandre, P., 2010. Mineralogy and geochemistry of the sodium metasomatism-related uranium occurrence of Aricheng South, Guyana. *Mineral. Deposita* 45, 351–367. <https://doi.org/10.1007/s00126-010-0278-7>.
- Arapov, J.A., Bojcov, V.J., Česnokov, N.I., Djakonov, A.V., Halbrštát, J., Jakovjenko, A.M., Kolek, M., Komínek, J., Kozyrev, V.N., Kremčukov, G.A., Lažanský, M., Milovanov, I.A., Nový, V., Šorf, F., 1984. Czechoslovak Uranium Deposits. SNTL, Prague (in Czech).
- Árkai, P., Máhlmann, R.F., Suchý, V., Balogh, K., Sýkorová, I., Frey, M., 2002. Possible effects of tectonic shear strain on phyllosilicates: a case study from the Kandersteg area, helvetic domain, Central Alps, Switzerland. *Schweiz. Miner. Petrog.* 82, 273–290. <https://doi.org/10.5169/seals-62365>.
- Banciu, H.L., Muntyan, M.S., 2015. Adaptive strategies in the double-extremophilic prokaryotes inhabiting soda lakes. *Curr. Opin. Microbiol.* 25, 73–79. <https://doi.org/10.1016/j.mib.2015.05.003>.
- Breiter, K., Sokol, A., 1997. Chemistry of the Bohemian granitoids. Geotectonic and metallogenic implications. *Sbor. Geol. Věd, LG* 31, 75–96.

- Cathelineau, M., 1986. The hydrothermal alkali metasomatism effects on granitic rocks: Quartz dissolution and related subsolidus changes. *J. Petrol.* 27, 945–965. <https://doi.org/10.1093/ptrology/27.4.945>.
- Charalambous, F.A., Ram, R., Pownceby, M.I., Tardio, J., Bhargava, S.K., 2012. Chemical and microstructural studies on natural and heat treated brannerite samples. *Min. Engin.* 39, 276–288. <https://doi.org/10.1016/j.mineng.2012.08.006>.
- Cuney, M., Emetz, A., Mercadier, J., Mykhaylov, V., Shunko, V., Yuslenko, A., 2012. Uranium deposits associated with Na-metasomatism from Central Ukraine: a review of some of the major deposits and genetic constraints. *Ore Geol. Rev.* 44, 82–106. <https://doi.org/10.1016/j.oregeorev.2011.09.007>.
- Cuney, M.L., Brouand, M., Cathelineau, M., Derome, M., Freiberg, R., Hecht, L., Kister, P., Lobaev, V., Lorilleux, G., Peiffert, C., Bastoul, A.M., 2003. What parameters control the high-grade-large tonnage of the proterozoic unconformity related uranium deposits? In: Cuney M. (ed.), *Int. Conf. Uranium Geochemistry 2003. Uranium deposits - Natural analogs-Environment*, 123–126. University Henri Poincaré, Nancy.
- Diessel, C.F.K., Öfler, R., 1975. Change in physical properties of coalified and graphitized phytoclasts with grade of metamorphism. *Neues Jb. Miner. Monat* 11, 11–26.
- Diessel, C.F.K., Brothers, R.N., Black, P.M., 1978. Coalification and graphitization in high-pressure schists in New Caledonia. *Contrib. Mineral. Petr.* 68, 63–78. <https://doi.org/10.1007/BF00375447>.
- Dill, H., Weiser, Th., 1981. Eine Molybdänsulfid-Impsonit-Mineralisation aus den Uranvorkommen Wäldel/Mähring (Oberpfalz). *N. Jb. Miner. Mh.* 10, 452–458.
- Dill, H.G., 1983. Vein- and metasedimentary-hosted carbonaceous matter and phosphorus from NE Bavaria (F.R. Germany) and their implication on syngenetic and epigenetic uranium concentration. *Neues Jb. Miner. Abh.* 148, 1–21.
- Dill, H., 1985. Die Vererzung am Westrand der Böhmisches Masse – Metalogenese in einer ensialischen Orogenzone. *Geol. Jahrb. Reihe D* 73, 1–461.
- Dill, H., 1986. Fault controlled uranium black ore mineralization from the western edge of the Bohemian Massif (NE-Bavaria, FR Germany), in: Fuchs H.D. (Ed.), *Vein-type uranium deposits*. Int. At. Energ. Agency, IAEA-TECDOC-316, pp. 303–323.
- Dill, H.G., Kus, J., Goldmann, S., Suárez-Ruiz, I., Neumann, T., Kaufhold, S., 2019. The physical-chemical regime of sulphide-bearing semi-graphite mineral assemblage in metabasic rocks (SE Germany) – a multidisciplinary study of the missing link between impsonite and graphite. *Int. J. Coal Geol.* 214, 103262. <https://doi.org/10.1016/j.coal.2019.103262>.
- Dörr, W., Zulauf, G., Fiala, J., Schastock, J., Scheuvs, D., Wulf, S., Vejnár, Z., Ahrendt, H., Wemmer, K., 1997. Dating of collapse related plutons along the West- and Central Bohemian shear zones (European Variscides). *Terra Nostra* 97, 31–35.
- Ferrari, A.C., Robertson, J., 2000. Interpretation of Raman spectra of disordered and amorphous carbon. *Phys. Rev. B* 61, 14095–14107. <https://doi.org/10.1103/PhysRevB.61.14095>.
- Fiala, V., 1980a. Die hydrothermale Verwandlung der Bor – Granits I. *Folia Mus. Ser. Nat. Boh. Occident. Geol.* 16, 1–28.
- Fiala, V., 1980b. Die hydrothermale Verwandlung der Bor – Granits II. *Folia Mus. Ser. Nat. Boh. Occident. Geol.* 17, 1–31.
- Flannery, E.N., George, S.C., 2014. Assessing the syngeneity and indigeneity of hydrocarbons in the ~1.4 Ga Velkerri Formation, McArthur Basin, using slice experiments. *Org. Geochem.* 77, 115–125. <https://doi.org/10.1016/j.orggeochem.2014.10.008>.
- Frost, B.R., 1988. A review of graphite-sulfide-oxide-silicate equilibria in metamorphic rocks. *Rendiconti Soc. Italiana Mineral. Petrol.* 43, 25–40.
- Frost, R.L., Reddy, J., 2011. Raman spectroscopy study of the uranyl titanate mineral brannerite (U, Ca, Y, Ce)₂(Ti, Fe)₂O₆: effect of metamictisation. *J. Raman. Spectr.* 42, 691–695. <https://doi.org/10.1002/jrs.2747>.
- Gautneb, H., Tveten, E., 2000. The geology, exploration and characterisation of graphite deposits in the Jennestad area, Vesterålen, northern Norway. *Norg. Geol. Unders. B.* 436, 67–74.
- Gopal, N.O., Narasimhulu, K.V., Lakshmana Rao, J., 2004. Optical absorption, EPR, infrared and Raman spectral studies of clinocllore mineral. *J. Phys. Chem. Solids* 65, 1887–1893. <https://doi.org/10.1016/j.jpcs.2004.07.003>.
- Hecht, L., Spiegel, W., Morteani, G., 1991. Multiphase alteration including disseminated uranium mineralization in quartz-depleted granites (episyenites) of the Fichtelgebirge (Northeastern Bavaria, Germany), in: Poty, B. (Ed.), *Source, Transport and Deposition of metals*. Proc. SGA Meeting, pp. 53–56.
- Hinrichs, R., Brown, M.T., Vasconcellos, M.A.Z., Abrashev, M.V., Kalkreuth, W., 2014. Simple procedure for an estimation of the coal rank using micro-Raman spectroscopy. *Int. J. Coal Geol.* 136, 52–58. <https://doi.org/10.1016/j.coal.2014.10.013>.
- Hoefs, J., 1997. *Stable Isotope Geochemistry*. Springer Verlag, Berlin.
- Holovka, D., Hnízdo E., 1992. Final report about exploration on uranium. Bor massif. DIAMO, Příbram. Unpublished report, pp. 1–280. (in Czech).
- ISO 7404-5, 2009. *Methods for the Petrographic Analysis of Coal – Part 5: Method of determining microscopically the reflectance of vitrinite*. International Organization for Standardization, Geneva, Switzerland (14 pp).
- Jacob, H., 1989. Classification, structure, genesis and practical importance of natural solid oil bitumen (“migrabitumen”). *Int. J. Coal Geol.* 11, 65–79.
- Jacob, H., 1993. Nomenclature, classification, characterization, and genesis of natural solid bitumen (migrabitumen). In: Parnel, J., Kucha, H., Landais, P. (Eds.), 1993. Springer-Verlag, Berlin, *Bitumens in Ore Deposits*, pp. 11–26.
- Jehlička, J., Bény, C., 1992. Application of Raman microspectroscopy in the study of structural changes in Precambrian kerogens during regional metamorphism. *Org. Geochem.* 2, 211–213. [https://doi.org/10.1016/0146-6380\(92\)90132-H](https://doi.org/10.1016/0146-6380(92)90132-H).
- Jehlička, J., Rouzard, J.N., 1990. Organic geochemistry of Precambrian shales and schists (Bohemian Massif, Central Europe). *Org. Geochem.* 16, 865–872. [https://doi.org/10.1016/0146-6380\(90\)90123-H](https://doi.org/10.1016/0146-6380(90)90123-H).
- Kafka, J., 2003. *Czech Ore and Uranium Mining Industry*. Anagram, Ostrava (in Czech).
- Křibek, B., 1981. The role of organic substances in the process of hydrothermal mineralization. *Geol. Capath.* 32, 605–614.
- Křibek, B., 1989. The role of organic matter in the metallogeny of the Bohemian Massif. *Econ. Geol.* 84, 1525–1540. <https://doi.org/10.2113/gsecongeo.84.6.1525>.
- Křibek, B., Hrabal, J., Landais, P., Hladíková, J., 1994. The association of poorly ordered graphite, coke and bitumens in greenschist facies rocks of the Ponikla group, Lucigum, Czech Republic: the results of graphitization of various types of carbonaceous matter. *J. Metamorph. Geol.* 12, 493–503. <https://doi.org/10.1111/j.1525-1314.1994.tb00038.x>.
- Křibek, B., Sýkorová, I., Machovič, V., Kněl, I., Laufek, F., Zachariáš, J., 2015. The origin and hydrothermal mobilization of carbonaceous matter associated with Paleoproterozoic orogenic-type gold deposits of West Africa. *Precambrian Res.* 270, 300–317. <https://doi.org/10.1016/j.precamres.2015.09.017>.
- Křibek, B., Sýkorová, I., Machovič, V., Laufek, F., 2008. Graphitization of organic matter and fluid-deposited graphite in Palaeoproterozoic (Birmian) black shales of Kaya-Goren greenstone belt (Burkina faso, West Africa). *J. Metamorph. Geol.* 26, 937–958. <https://doi.org/10.1111/j.1525-1314.2008.00796.x>.
- Křibek, B., Žák, K., Dobeš, P., Leichmann, J., Pudilová, M., René, M., Scharm, B., Scharmová, M., Hájek, A., Holeczy, D., Hein, U.F., Lehmann, B., 2009. The Rožná uranium deposit (Bohemian Massif, Czech Republic): shear zone-hosted, late Variscan and post-Variscan hydrothermal mineralization. *Mineral. Deposita* 44, 99–128. <https://doi.org/10.1007/s00126-008-0188-0>.
- Křibek, B., Žák, K., Spangenberg, J.E., Jehlička, J., Prokeš, S., Komínek, J., 1999. Bitumens in the late Variscan hydrothermal vein-type uranium deposit of Příbram, Czech Republic; sources, radiation-induced alteration, and relation to mineralization. *Econ. Geol.* 94, 1093–1114. <https://doi.org/10.2113/gsecongeo.94.7.1093>.
- Kropotova, O.N., Milovska, A.B., Čech, F., 1976. Isotopic composition of carbon of the some graphites. *Vest. Moscov. Univ.* 1976 (2), 66–71 (in Russian).
- Kwicińska, B., Petersen, H.I., 2004. Graphite, semi-graphite, natural coke, and natural char classification – ICCP system. *Int. J. Coal Geol.* 57, 99–116. <https://doi.org/10.1016/j.coal.2003.09.003>.
- Kyser, T.K., Wilson, M.R., Ruhmann, G., 1989. Stable isotope constraints on the role of graphite in the genesis of unconformity-type uranium deposits. *Can. J. Earth Sci.* 26, 490–498. <https://doi.org/10.1139/e89-042>.
- Luo, G., Hallmann, C., Xie, S., Ruan, X., Summons, R.E., 2015. Comparative microbial diversity and redox environments of black shale and stromatolite facies in the Mesoproterozoic Xiamaling Formation. *Geochim. Cosmochim. Acta.* 151, 150–167. <https://doi.org/10.1016/j.gca.2014.12.022>.
- Macmillan, E., Cook, N.J., Ehrig, K., Pring, A., 2017. Chemical and textural interpretation of late-stage coffinite and brannerite from the Olympic Dam IOCG-Ag-U deposit. *Miner. Mag.* 81, 1323–1366. <https://doi.org/10.1180/minmag.2017.081.006>.
- Manara, D., Renker, B., 2003. Raman spectra of stoichiometric and hyperstoichiometric uranium dioxide. *J. Nucl. Mater.* 321, 233–237. [https://doi.org/10.1016/S0022-3115\(03\)00248-4](https://doi.org/10.1016/S0022-3115(03)00248-4).
- Mrázek, P., Fiala, V., 1979. Die hydrothermalen Verwandlungsminerale der Lagerstätte Zadní Chodov. *Folia Mus. Ser. Nat. Boh. Occid. Geologica* 14, 1–15.
- Novák, J., Paška, R., 1983. Final report about exploration of the Eastern Shear-Zone on the Zadní Chodov-Eastern uranium deposit. Uranium industry, Příbram. Unpublished report pp.1–56. (in Czech).
- OECD-IAEA, 2003. *Uranium 2003: Resources, Production and Demand*. Nuclear Energy Agency (NEA) of the Organization for Economic Co-operation and Development (OECD) and the United Nation's International Atomic Energy Agency (IAEA).
- Oohashi, K., Hirose, T., Shimamoto, T., 2011. Shear-induced graphitization of carbonaceous materials during seismic fault motion: Experiments and possible implications for fault mechanics. *J. Struct. Geol.* 33, 1122–1134. <https://doi.org/10.1016/j.jsg.2011.01.007>.
- Ordynec, G.E., Komínek, J., Anderson, E.B., Milovanov, I.A., Nikolsky, A.L., Romanidis, K., 1987. Alters of the uranium mineralization of deposits at the West-Bohemian ore district. *Geol. Hydrometall. Uranu* 11, 23–64 (in Czech).
- Otto, A., Simoneit, B.R.T., 2002. Biomarkers of Holocene buried conifer logs from Bella Coola and north Vancouver, British Columbia, Canada. *Org. Geochem.* 33, 1241–1251. [https://doi.org/10.1016/S0146-6380\(02\)00139-0](https://doi.org/10.1016/S0146-6380(02)00139-0).
- Pauling, L., 1966. The structure and properties of graphite and boron nitride. *Proc. Nat. Acad. Sci.* 56, 1646–1652.
- Pawlowska, M.M., Butterfield, N.J., Brocks, J.J., 2013. Lipid taphonomy in the Proterozoic and the effect of microbial mats on biomarker preservation. *Geology* 41, 103–106. <https://doi.org/10.1130/G33525.1>.
- Peters, K.E., Walters, C.C., Moldowan, J.M., 2005. *The Biomarker Guide*. Cambridge University Press.
- Polito, P.A., Kyser, T.K., Stanley, C., 2009. The Proterozoic, albitite-hosted, Valhalla uranium deposit, Queensland, Australia: a description of the alteration assemblage associated with uranium mineralisation in diamond drill hole V39. *Mineral. Deposita* 44, 11–40. <https://doi.org/10.1007/s00126-007-0162-2>.
- Poty, B., Leroy, J., Cathelineau, M., Cuney, M., Friedrich, M., Lespinasse, M., Turpin, L., 1986. Uranium deposits spatially related to granites in the French part of the Hercynian Orogen. In: Fuchs, H. (Ed.), *Vein Type Uranium Deposits*. Int. At. Energ. Agency, IAEA-TECDOC-316, pp. 215–260.
- Pouchou, J.L., Pichoir, F., 1985. “PAP” (ρ-ρ-Z) procedure for improved quantitative microanalysis. In: Armstrong, J.T. (Ed.), *Microbeam Analysis*. San Francisco Press, San Francisco, pp. 104–106.
- René, M., Dolníček, Y., 2017. Uraninite, coffinite and brannerite from shear-zone hosted uranium deposits of the bohemian massif (central european variscan belt). *Minerals* 7, 50. <https://doi.org/10.3390/min7040050>.
- René, M., 2017. Alteration of granitoids and crystalline rocks and uranium mineralisation in the Bor pluton area, Bohemian Massif, Czech Republic. *Ore Geol. Rev.* 81, 188–200. <https://doi.org/10.1016/j.oregeorev.2016.09.033>.
- Reutel, Ch., 1992. *Krustenfluide in Gesteinen und Lagerstätten am Westrand der Böhmisches Masse*. Göttinger Arbeiten Geol. Paläontol. 53, 1–75.

- Robert, P., 1988. Organic Metamorphism and Geothermal History. Elf-Aquitane and D. Reidel, Dordrecht Boston, pp. 1–311.
- Rodrigues, S., Suárez-Ruiz, I., Marques, M., Camean, I., Flores, D., 2011. Microstructural evolution of high temperature treated anthracites of different rank. *Int. J. Coal Geol.* 87, 204–211. <https://doi.org/10.1016/j.coal.2011.06.009>.
- Rodrigues, S., Suárez-Ruiz, I., Margues, M., Flores, D., 2012. Catalytic role of mineral matter in structural transformation of anthracites during high temperature treatment. *Int. J. Coal Geol.* 93, 49–55. <https://doi.org/10.1016/j.coal.2012.01.012>.
- Rudorff, W., Stump, E., Spriessler, W., Siecke, F.W., 1963. Reaktionen des Graphite mit Metallchloriden. *Angew. Chem.* 75, 130–136. <https://doi.org/10.1002/ange.19630750204>.
- Schiffbauer, J.D., Yin, L., Bodnar, R.J., Kaufman, A.J., Meng, F., Hu, J., Shen, B., Yuan, X., Bao, H., Xiao, S., 2007. Ultrastructural and geochemical characterization of archean-Paleoproterozoic graphite particles: implications for recognizing traces of life in highly metamorphosed rocks. *Astrobiology* 7, 684–704. <https://doi.org/10.1089/ast.2006.0098>.
- Siebel, W., Trzebski, R., Stettner, G., Hecht, L., Casten, U., Höhndorf, A., Müller, P., 1997. Granitoid magmatism of the NW Bohemian Massif revealed: gravity data, composition, age relations and phase concept. *Geol. Rdsch Suppl.* 86, 45–63. <https://doi.org/10.1007/PL00014665>.
- Smith Jr., D.K., 1984. Uranium mineralogy. In: deViv, B., Ippolito, F., Capaldi, G., Simpson, P.R. (Eds.), *Uranium Geochemistry, Mineralogy, Geology, Exploration and Resources*. The Institution of Mining and Metallurgy, London, pp. 43–88.
- Suchý, V., Frey, M., Wolf, M., 1997. Vitrinite reflectance and shear-induced graphitization in orogenic belts: a case study from Kandersteg area, Helvetic Alps. Switzerland. *Int. J. Coal Geol.* 34, 1–20. [https://doi.org/10.1016/S0166-5162\(97\)00018-9](https://doi.org/10.1016/S0166-5162(97)00018-9).
- Suchý, V., Sýkorová, I., Melka, K., Filip, J., Machovič, V., 2007. Illite “crystallinity”, maturation of organic matter and microstructural development associated with lowest-grade metamorphism of Neoproterozoic sediments in the Teplá-Barrandian unit, Czech Republic. *Clay Miner.* 42, 503–526. <https://doi.org/10.1180/claymin.2007.042.4.08>.
- Sun, M., Wakeham, S.G., Lee, C., 1997. Rates and mechanisms of fatty acid degradation in oxic and anoxic coastal marine sediments of Long Island Sound, New York. USA. *Geochim. Cosmochim. Ac.* 61, 341–355. [https://doi.org/10.1016/S0016-7037\(96\)00315-8](https://doi.org/10.1016/S0016-7037(96)00315-8).
- Sýkorová, I., Křibek, B., Havelcová, M., Machovič, V., Špaldoňová, A., Lapčák, L., Kněl, I., Blažek, J., 2016. Radiation- and self-ignition induced alterations of Permian uraniumiferous coal from the abandoned “Novátor” mine waste dump (Czech Republic). *Int. J. Coal Geol.* 168, 162–178. <https://doi.org/10.1016/j.coal.2016.08.002>.
- Topp, J., 1993. Flüssigkeitseinschluss-Untersuchungen am Bohrkernmaterial der KTB bis 4000 Meter. *Göttinger Arb. Geol. Paläont.* 61, 1–58.
- Tuinstra, F., Koenig, J.L., 1970. Raman spectrum of graphite. *J. Chem. Phys.* 53, 1126–1131. <https://doi.org/10.1063/1.1674108>.
- Volkenstein, F.F., 1960. *Elektronaja Teorija Kataliza*. Fizmatizdat, Moskva.
- Wada, H., Tomita, T., Matsuura, K., Iuchi, K., Ito, M., Mirikiyo, T., 1994. Graphitization of carbonaceous matter during metamorphism with references to carbonate and polytic rocks of contact and regional metamorphisms, Japan. *Contrib. Miner. Petrol.* 118, 217–228.
- Walshe, J.L., 1986. A six-component chlorite solid solution model and the conditions of chlorite formation in hydrothermal and geothermal systems. *Econ. Geol.* 81, 681–703. <https://doi.org/10.2113/gsecongeo.81.3.681>.
- Walther, J., Althaus, 1988. Origin of differential fluid pressures in the course of a metamorphic event. *KTB Report* 88–10, 62.
- Wang, A., Dhamenincourt, P., Dubessy, J., Guerdard, D., Landais, P., Lelaurain, M., 1989. Characterization of graphite alteration in a uranium deposit by micro-Raman spectroscopy, X-ray diffraction, transmission electron microscopy and scanning electron microscopy. *Carbon* 27, 209–218. [https://doi.org/10.1016/0008-6223\(89\)90125-5](https://doi.org/10.1016/0008-6223(89)90125-5).
- Wang, Y., Fang, X., Zhang, T., Li, Y., Wu, Y., He, D., Wang, Y., 2010. Predominance of even carbon-numbered n-alkanes from lacustrine sediments in Linxia Basin, NE Tibetan Plateau: implications for climate change. *Appl. Geochem.* 25, 1478–1486. <https://doi.org/10.1016/j.apgeochem.2010.07.002>.
- Wilde, A., Otto, A., Jory, J., MacRae, C., Pownceby, M., Wilson, N., Torpy, A., 2013. Geology and mineralogy of uranium deposits from Mount Isa, Australia: implications for albitite uranium deposit models. *Minerals* 3, 258–283. <https://doi.org/10.3390/min303>.
- Wopenka, B., Pasteris, J.D., 2005. A mineralogical perspective on the apatite in bone. *Mater. Sci. Eng. C* 25, 131–143. <https://doi.org/10.1016/j.msec.2005.01.008>.
- Wopenka, B., Pasteris, J.D., 1993. Structural characterization of kerogens to granulite-facies graphite: applicability of Raman microprobe spectroscopy. *Am. Mineral.* 78, 533–557.
- Zhang, Y., Karatchevseva, I., Qin, M., Middleburgh, S.C., Lumpkin, G.R., 2013. Raman spectroscopic study of natural and synthetic brannerite. *J. Nucl. Mat.* 437, 149–153. <https://doi.org/10.1016/j.jnucmat.2013.02.004>.
- Ziegenbein, D., Johannes, W., 1990. Graphit-Fluid-Wechselwirkungen: Einfluss der Graphitkristallinität. *KTB Report* 90-4, 559.
- Ziegenbein, D., Skrotzki, W., Hoefs, J., Müller, H., Reutel, Chr., Emmermann, R., 1989. *Fluidtransport und Graphitbildung auf Störungszonen*. *KTB Report* 89-3, 46–53.
- Zulauf, G., 1994. Ductile normal faulting along the West Bohemian Shear Zone (Moldanubian/Tepla-Barrandian boundary): evidence for late Variscan extensional collapse in the Variscan Internides. *Geol. Rundsch.* 83, 276–292. <https://doi.org/10.1007/BF00210545>.